

# Determination of Matter Surface Distribution of Neutron-rich Nuclei

Akihisa KOHAMA <sup>1</sup> \*; Ryoichi SEKI <sup>2,3</sup>, Akito ARIMA <sup>4</sup>,  
and Shuhei YAMAJI <sup>1</sup>

<sup>1</sup> RIBF Project Office, Cyclotron Center,  
RIKEN (The Institute of Physical and Chemical Research),  
2-1 Hirosawa, Wako-shi, Saitama 351-0198, JAPAN

<sup>2</sup> Department of Physics and Astronomy,  
California State University, Northridge, CA 91330, USA

<sup>3</sup> W. K. Kellogg Radiation Laboratory,  
California Institute of Technology, Pasadena, CA 91125, USA

<sup>4</sup> The House of Councilors, 2-1-1 Nagata-cho, Chiyoda-ku, Tokyo 100-8962, JAPAN

October 25, 2018

## Abstract

We demonstrate that the matter density distribution in the surface region is determined well by the use of the relatively low-intensity beams that become available at the upcoming radioactive beam facilities. Following the method used in the analyses of electron scattering, we examine how well the density distribution is determined in a model-independent way by generating pseudo data and by carefully applying statistical and systematic error analyses. We also study how the determination becomes deteriorated in the central region of the density, as the quality of data decreases. Determination of the density distributions of neutron-rich nuclei is performed by fixing parameters in the basis functions to the neighboring stable nuclei. The procedure allows that the knowledge of the density distributions of stable nuclei assists to strengthen the determination of their unstable isotopes.

*PACS:* 21.10.Gv, 24.10.Ht, 25.40.Cm, 29.85.+c

*Keywords:* unstable nuclei, matter density distribution, proton-nucleus elastic scattering, model-independent determination.

---

\*Permanent Address: RI Beam Science Laboratory, RIKEN. e-mail: kohama@rarfaxp.riken.go.jp

# 1 Introduction

Experimental facilities for unstable nuclei are receiving much attention in the recent years. Radioactive Ion Beam Factory (RIBF) is under construction at RIKEN in Japan, and Rare Isotope Accelerator (RIA) facility is being proposed in USA. The facilities are expected to provide much data which are expected to reveal interesting properties and dynamics of unstable nuclei [1, 2]. Among various properties, one property of interest is the one-body matter density distribution. The density distribution is a fundamental quantity of nuclei and serves as an important measure to test how well we understand nuclear structure [3], and will be experimentally investigated at an early stage after completion of the facilities. It is perhaps an appropriate time to make a close investigation how well one could determine the one-body matter density distributions from the data expected to emerge from the facilities. As a concrete example, we examine the type of the experiments under consideration at the RIBF.

Unstable nuclei of neutron-rich side (neutron-rich nuclei) are often characterized as those with a large surface region generated by loosely bound valance nucleons [4, 5, 6, 7]. We will give a special attention to the determination of the matter density distributions in the surface region, though we will have to treat, of course, the entire region of nuclei. The surface is the region where  $\rho(r) / \rho(0)$  varies from 0.9 to 0.1 if we have a density distribution of monotonically decreasing function in  $r$ , such as the Woods-Saxon density, in mind [8]. More elaborated definitions of the surface can be found in the literature [9].

In this work, we focus on the question, how the precision in the determination of the matter density distributions of neutron-rich nuclei is related to the accuracy of experimental data, specifically of proton-nucleus elastic scattering differential cross sections. For the purposes of making the examination definitive, we perform a model calculation, by artificially generating data from given density distributions and then by making their statistical analysis.

The question which we address is an old problem, and the basic method that we use has been well developed for extracting nuclear charge density distributions from high-energy electron scatterings and muonic atom data over years [10, 11, 12, 13]. We make no new contribution to the method, but apply it to the determination of the nuclear matter density distributions, focusing on the surface region of neutron-rich nuclei. As we discuss in the next section, the method has been applied to the determination of the nuclear matter density distributions but with less rigor, and no use has been made to the case of neutron-rich nuclei. The present work is novel in the careful examination of how the method is applied to the nuclear-matter-density-distribution problem.

In this work, we follow the traditional approach of the least-square method [14] and do not discuss other approaches often referred to as Bayesian methods, such as maximum entropy technique. These approaches involve issues of subjectivity [14, 15], and require a separate study. We are currently investigating their relevance to our problem.

The contents of this paper are as follows: We describe our approach in comparison to previous works in Section 2, and the formalism used in our analysis in Section 3. There, we introduce pseudo data in Subsection 3.2 and error estimate in Subsection 3.3. Numerical results are presented in Section 4, including discussions of pseudo data in Subsection 4.2 and those of error estimate in Subsections 4.1 and 4.3. We summarize our results in Section 5. Appendices include a brief discussion of basis functions in Appendix A, a list of the expressions for the density and the data in Appendix B, and a summary of formula and numerical results concerning the Fourier-Bessel basis functions in Appendix C.

Some preliminary results of this work have been previously reported [16]. This paper provides a full account of our work <sup>1</sup>. The major added contents are the discussion of the completeness error, the way how to generate pseudo data, and the other confirmation of the fitted results with the use of the  $\chi^2$ -distribution. We have also added several Appendices to the previous report.

---

<sup>1</sup>This paper is the revised version of the preprint, RIKEN-AF-NP-413, Nov., 2001, with the same authors.

## 2 Overview of Our Approach

In this investigation, the density distributions are determined in a “model-independent” way. As the model-independent determination is the central feature of our procedure, we wish to clarify at the outset what we mean by the model-independent procedure. It is model-independent, because the density distribution is determined as a linear combination of basis functions. We do this by avoiding the use of specific analytic forms of the density distribution, which is the common practice in this field [10, 11, 12, 13].

We will explicitly assume, however, that the density distribution is directly related to the differential cross sections through the eikonal approximation in the lowest-order optical potential, so-called  $t$ - $\rho$  form [17]. We assume this because of convenience and simplicity. The assumption is basically independent of our semi-quantitative conclusion on the question of how the density determination depends on experimental accuracy. That is, we expect that the same conclusion would emerge if we were to adopt a more elaborate relation. We emphasize that the issue we wish to address in this paper is this question of the dependence of the density *determination* on the experimental *accuracy*, not on the relation between the density and the cross section themselves.

The elastic scattering cross section data that we will examine in our model calculation are generated artificially, and will be referred to as “pseudo data” [13, 18, 19, 20]. At first, they are generated from a specific density distribution (of the three-parameter Fermi form, Eq. (4.1)) by the use of the above described procedure with the eikonal approximation and are then shuffled statistically at each data point with an assigned experimental uncertainty (corresponds to a Gaussian width), simulating the situations expected in future experiments at the RIBF. We will prepare 25 sets of such shuffled data, each of which yields the best-fit density distribution with its uncertainty. The originally assumed density distribution is taken to be the true density distribution. The average of the density distributions determined will be close to the true distribution, and their deviations from the average will give us the statistical uncertainty associated with the model-independent determination [14]. The difference between the true and averaged distributions corresponds to the systematic uncertainty [14]. The systematic uncertainty corresponds to the limitation of the model-independent procedure associated with our (model-independent) representation of the density distribution. The systematic uncertainty could also include the uncertainty associated with the relation between the density distribution and the differential cross sections. In this work, we will not examine this part of the systematic uncertainty by applying the same relation for generating the data and fitting to them.

We apply a particular combination of Gaussian functions [21] as a model-independent representation of the density distribution. We do this for simplicity and for stability of computation, but a particular choice of the basis should not alter the final conclusion. That is, the nuclear density distribution determined at the end should fall in within the systematic error that is noted above. We will confirm this by comparing the results of our Gaussian basis functions with those of the more established Fourier-Bessel basis [13].

There are several well-known basis functions. The expansion in terms of  $\delta$ -functions was proposed originally by Lenz [22], and extended by Lenz and Friedrich [23]. Since the early 70’s, Sick and his collaborators have been analyzing the electron scattering data using another set of Gaussian basis functions, the expansion in a sum of Gaussians (SOG) [24], with great success [12, 25, 26]. These Gaussian basis functions are a series of Gaussians of multi-center. With their analyses, they demonstrated that the determinations of the charge density distributions by the phase-shift analyses is reliable and accurate by comparing the electron-nucleus with the positron-nucleus elastic scattering [25], and the charge density distributions of  $^{208}\text{Pb}$  was determined with an uncertainty of the order of  $\Delta\rho(r)/\rho(r) = \pm 1$  [%] [26]. Recently, Burov *et al.* analyzed the electron scattering data by expanding the density distribution in terms of the symmetric Fermi distribution [27] and its derivative series [28].

The three-parameter Fermi distribution that we use mimics the matter density distribution of  $^{58}\text{Ni}$  and the relativistic mean field result mimics that of  $^{78}\text{Ni}$ , which we chose as examples of stable and unstable nuclei, respectively. We assume here that the matter density distribution of  $^{58}\text{Ni}$  behaves similarly to its charge density. From the intense studies of the charge density distribution [29, 30], it was found that the charge density of  $^{58}\text{Ni}$  shows the less oscillating structure than the predictions of Hartree-Fock calculations [30]. This validates our choice of this simple functional form (See also

in Appendix B). The pseudo data are generated for the proton incident energy of 1.047 [GeV]. The energy is chosen to be the same as that of the proton-nucleus scattering experiments at SATURN, Saclay [31, 32, 33], because the experimental data and their analyses have shown that the eikonal approximation yields reasonably realistic results (See Fig. 1 in the next section).

In this work, we assume that the proton-nucleus elastic scattering differential cross sections and the nuclear density distribution are exactly related by the eikonal approximation with the  $t$ - $\rho$  form. With this simple form, one can see analytically that the nuclear radius determines the oscillation and the diffuseness does the exponential decrease with momentum transfer of the elastic cross section [34]. This helps one to obtain the insight to the relation between the quality of data and the fitted density distributions. Of course, the eikonal approximation is an approximation, and the degree of its validity is sometimes questioned, especially when it is used with the  $t$ - $\rho$  form. It can be numerically improved by the use of the partial-wave decomposition method, and the  $t$ - $\rho$  form can be also improved by incorporating higher-order effects into the potential. Our objective of finding the relation between the precision of the density determination and the experimental accuracy certainly depends on how reliably the density and the data are related each other. For the sake of making our examination as clear as possible, however, we isolate the issue of the precision-accuracy in this model calculation, by artificially assuming the density-data relation to be exact. In realistic model-independent analyses of actual experimental data, we must address the latter issue and take account of the reliability of the relation of the two quantities.

Once the density-data relation is assumed to be exact, the model-independent analysis can provide a definitive result for the precision-accuracy issue at any energy. The result will become, however, unrealistic as we go down in the energy. For a model calculation at lower energies, such as those around 500 [MeV] where various experiments are being planned at the RIBF, it would be desirable to use more rigorous relation based on the partial-wave decomposition and an improved optical potential. We are planning to extend the present work to these energies by the use of partial-wave decomposition.

There have been efforts on the determination of the nuclear (matter-) density distributions [10, 35, 36, 37], which are, of course, founded on the charge density studies. As reviewed by Alkhozov *et al.* [36] and by Chaumeaux *et al.* [37] in 1978, and by Batty *et al.* [10] in 1989, some works include model-independent analyses of the experimental data: after the first attempt of the model-independent approach to the matter density distributions by Brissaud *et al.* [38], Ray *et al.* [39, 40], Hoffmann *et al.* [41], and Alkhozov *et al.* [32] studied the matter density distributions along similar lines. More recent work is by Starodubsky *et al.* [42]. Gils *et al.* analyzed the data of the  $\alpha$ -nucleus elastic scattering, and obtained the quite similar surface density distribution as those from the proton-nucleus scattering data within the statistical uncertainties [43]. None of these works has addressed, however, the issue of determination of the surface density distribution associated with nuclei near the drip lines. The recent analysis by Alkhozov *et al.* [44] of the GSI experiment of helium isotope addresses this issue, but it is a model-dependent analysis and its conclusion is in question under the light of a model-independent analysis [45].

Our work is the first model calculation that examines closely the information content of the experimental data, including the question of the *systematic* error as well as the statistical error, in the model-independent approach.

Although they are model-dependent, the matter density distributions of neutron-rich nuclei have been deduced recently, *e.g.* from the low-energy proton elastic and inelastic scattering [46, 47], and from the interaction cross sections [48, 49, 50].

### 3 Formalism

#### 3.1 Fitting Procedure

For the sake of notations and completeness, we outline our formalism in this section. It is basically the same as that in the review article by Friar and Negele [13]. The formalism itself was studied also in detail by Dreher *et al.* [18].

We approximately express the one-body matter density distribution that is assumed to be true,  $\rho_{\text{true}}(\mathbf{r})$ , in  $M$ -terms of basis functions,  $f_n(\mathbf{r})$ , ( $n = 1, \dots, M$ ):

$$\rho_{\text{true}}(\mathbf{r}) \simeq \rho_M^{\text{fit}}(\mathbf{r}) \equiv \sum_{n=1}^M C_n f_n(\mathbf{r}), \quad (3.1)$$

where  $\rho_M^{\text{fit}}(\mathbf{r})$  is the fitted density distribution. Here, as we do not use a particular analytical functional form of the density, our approach is model-independent. Strictly speaking, there is no completely model-independent approach, because the basis functions include parameters to be chosen and only a finite number ( $M$ ) of the basis functions can be used. The systematic errors are generated due to this incomplete model-independence of the approach. We will describe this point fully later.

For simplicity, we assume that the nuclei are not deformed and examine only the radial dependence of their distributions. The deformation can be treated in a similar model-independent way, but will make the procedure more complicated. The fitted density is normalized to the mass number,  $A$ , as

$$\int d\mathbf{r} \rho_M^{\text{fit}}(r) = 4\pi \int_0^\infty r^2 dr \rho_M^{\text{fit}}(r) = A. \quad (3.2)$$

The expansion coefficients,  $\{C_n\}$ , are determined by minimizing

$$\chi^2(\{C_n\}) = \sum_{\alpha=1}^{N_{\text{data}}} \frac{1}{\epsilon_\alpha^2} \left( \frac{d\sigma_\alpha^{\text{data}}}{d\Omega} - \frac{d\sigma_\alpha^{\text{fit}}}{d\Omega}(\{C_n\}) \right)^2, \quad (3.3)$$

under the variations of the finite set  $\{C_n\}$ . Here,  $d\sigma_\alpha/d\Omega$ 's are the differential cross sections of proton-nucleus elastic scattering at the center-of-mass angle,  $\theta_\alpha$ .  $N_{\text{data}}$  is the number of data points, and  $\epsilon_\alpha$  is the uncertainty or error associated with the data at  $\theta_\alpha$ .  $d\sigma_\alpha^{\text{data}}/d\Omega$ 's are the pseudo data that we generate, and  $d\sigma_\alpha^{\text{fit}}/d\Omega(\{C_n\})$ 's are those calculated from the fitted density distribution. We carry out all least-square minimization using MINUIT [51] in the CERN Library.

The dependence of  $d\sigma_\alpha^{\text{fit}}/d\Omega$  on  $\{C_n\}$  involves complicated physics. In this work, we use the first-order optical potential in the Glauber approximation, which establishes the relation between the nuclear density and the differential cross section [17]. The relation is well known, but we list some of basic formulae in the relation in Appendix B for completeness and clarification. As noted in Section 2, we assume the relation to be exact and generate pseudo data using it. No real experimental differential cross section datum enters our calculation and its analysis. As such, it is logically immaterial how reliable the relation itself is, but it becomes an issue how realistic or relevant to future experiments.

Figure 1 compares the real experimental data of proton-<sup>58</sup>Ni elastic scattering cross sections at 1.047 [GeV] from SATURN, Saclay [31, 32, 33] with the calculation. Note that in our later model calculations, we will use the same nuclear density at the same kinetic energy as used here. Agreement between the data and the calculation is not too great, but is not too much off either. The agreement could be improved by including the Coulomb interaction and also various higher-order corrections, such as the center-of-mass correction and nuclear correlation [17, 52]. The improvement would reduce the unpleasant sharp dips in the differential cross sections [34, 53] and is certainly desirable, but again, is not essential to our model calculations.

As the basis functions of Eq. (3.1), we use Gaussian basis functions with a cut off at  $R$ :

$$f_n(r) = \exp(-r^2/r_n^2) \theta(R - r), \quad (n = 1, \dots, M), \quad (3.4)$$

where  $r_n$  is the size parameter, defined in the geometrical progression,  $r_n = r_1 a^{n-1}$  ( $n = 1, \dots, M$ ) [21]. These Gaussian basis functions differ from those used previously by Sick [24], and will be referred

to as ‘‘Kamimura-Gauss basis functions’’ after the author who used them extensively [21]. We list the basic formulae of the Kamimura-Gauss basis functions in Appendix A.

In Subsection 4.1 we will show that the completeness error defined in Subsection 3.3 of the Kamimura-Gauss basis functions is very small, which is the same order of magnitude as that of the Fourier-Bessel ones shown in Appendix C.

## 3.2 Pseudo data

We create the total 25 sets of the pseudo data. We choose the number of 25 as the minimum number for statistical discussions. Each set mimics a series of experimental data obtained by an experiment, and consists of the proton-nucleus elastic scattering cross sections at the center-of-mass scattering angles that are common to all pseudo-data set. No Coulomb interaction is included, for simplicity.

The application of the pseudo data to estimate the density distributions is not new [13, 18]. In this work we study how far we can access the matter density distributions with varying the nuclear beam intensity, having in mind the neutron-rich nuclei. This is new.

At each scattering angle,  $\theta_\alpha$ , we thus generate 25 cross sections. They are generated artificially, but as realistically as possible. The following steps are taken to achieve this objective. First, we calculate the ‘‘true’’ cross section,  $d\sigma_\alpha^{\text{true}}/d\Omega$ , from the given nuclear density of a three-parameter Fermi distribution form, as described in Appendix B. Second, a set of 25 cross sections are generated, randomly distributed about each ‘‘true’’ cross section. Third, an uncertainty is assigned to each datum generated.

Let us elaborate on these steps. In the second step, 25 cross sections are generated following the Gaussian distribution,

$$f(x; \mu, \sigma^2) = \frac{1}{\sqrt{2\pi\sigma^2}} \exp\left\{-\frac{(x - \mu)^2}{2\sigma^2}\right\} \quad (3.5)$$

where

$$\mu = \frac{d\sigma_\alpha^{\text{true}}}{d\Omega}, \quad (3.6)$$

$$\sigma = \mu / \sqrt{N_{\text{yield}}(\theta_\alpha)}. \quad (3.7)$$

Here, we define the yield count,

$$N_{\text{yield}}(\theta_\alpha) = \frac{N_0}{B_0} \frac{d\sigma_\alpha^{\text{true}}}{d\Omega}, \quad (3.8)$$

where  $B_0/N_0$  [mb/str] is the yield parameter, which is the magnitude of the cross section that yields a unit count in the measurement. We set  $N_0 = 10$ , so that

$$\sigma = 0.316\mu, \quad \text{when} \quad \frac{d\sigma_\alpha^{\text{true}}}{d\Omega} = B_0, \quad (3.9)$$

and we examine three cases of  $B_0 = 0.1, 1.0,$  and  $10.0$  [mb/str]. Note that the datum less than  $B_0/N_0$  is rejected, because  $N_{\text{yield}}(\theta_\alpha)$  of Eq. (3.8) becomes less than one.

In the third step, we assign an uncertainty to each pseudo datum, using the expression of  $\sigma$  in Eq. (3.7) with Eq. (3.8), except for  $d\sigma_\alpha^{\text{true}}/d\Omega$  being replaced by the pseudo datum itself.

The center-of-mass scattering angle is taken to be greater than  $4^\circ$ , based on the expected experimental setups (of the inverse kinematics) at the RIBF. The set of the angles,  $\{\theta_\alpha\}$ , is chosen with  $1.0^\circ$  separations, but the separation is reduced near the forward direction as described in Appendix D. The number of the angles (and thus the number of the data in each pseudo-data set,  $N_{\text{data}}$ ) is then made to be more than 20, which provides the number of degrees of freedom,  $N_{\text{dof}} (\equiv N_{\text{data}} - M)$ , suitable for the least-square fitting procedure that we will carry out for  $M = 10$ .

The pseudo data are generated by following the above recipe, as will be described in Subsection 4.2.

### 3.3 Errors and Uncertainties

In this subsection we discuss how to estimate the errors involved in the determination of density distributions. There are three kinds of errors; the completeness error, the systematic error, and the statistical error [13].

#### 3.3.1 Completeness Error

The completeness error is a measure of how closely the density distribution is reconstructed by the use of a finite number of the basis functions [13]. We introduce the relative completeness error as

$$\Delta\rho_M^{\text{com}}(r) \equiv |\rho_{\text{true}}(r) - \tilde{\rho}_M(r)| / \rho_{\text{true}}(r), \quad (3.10)$$

where

$$\tilde{\rho}_M(r) = \sum_{n=1}^M \tilde{C}_n f_n(r). \quad (3.11)$$

$\{\tilde{C}_n\}$  is determined to minimize  $(\rho_{\text{true}}(r) - \tilde{\rho}_M(r))^2$  under the variations of  $\tilde{C}_n$ 's. Note that  $f_n(r)$ 's are linearly independent set, but are not necessarily orthogonal among each other. Since we use a finite number of the basis functions, the completeness of the set is not the issue here.

$\{\tilde{C}_n\}$  is given by

$$\tilde{C}_m = \sum_{n=1}^M F_{m,n}^{-1} v_n, \quad (3.12)$$

as the solution of

$$\sum_{m=1}^M F_{n,m} \tilde{C}_m = v_n, \quad (3.13)$$

where

$$F_{n,m} \equiv 4\pi \int_0^\infty r^l dr f_n(r) f_m(r), \quad (3.14)$$

$$v_n \equiv 4\pi \int_0^\infty r^l dr f_n(r) \rho_{\text{true}}(r). \quad (3.15)$$

Here,  $l$  is the phase-volume parameter to specify the relationship among the basis functions, as described in Appendix A. In this work, we choose  $l = 0$ .

The relative completeness error introduced here will provide a useful means for assessing how well the surface distribution is determined. In this work, we use the Kamimura-Gauss basis functions for  $\{f_n(r)\}$ .

#### 3.3.2 Statistical Uncertainties and Systematic Errors

When the true value,  $X_{\text{true}}$ , is known, the mean square error of a measured value,  $X_{\text{data}}$ , is defined as [14],

$$\langle (X_{\text{data}} - X_{\text{true}})^2 \rangle = \langle (X_{\text{data}} - \langle X_{\text{data}} \rangle)^2 \rangle + (\langle X_{\text{data}} \rangle - X_{\text{true}})^2, \quad (3.16)$$

$$\equiv \sigma^2 + b^2, \quad (3.17)$$

where the bracket,  $\langle A \rangle$ , implies the sample mean of  $A$ .  $\sigma$  is the statistical error, and  $b$  is the systematic error or the bias. Generally, the error contained in data is an independent sum of the statistical and systematic errors. The statistical error shows how large the fitted results fluctuate around the sample mean, while the systematic error shows the deviation of the sample means from the true value [14].

In our case, the statistical error of the fitted cross sections at a  $\theta_{\text{cm}}$  is

$$\sigma_X^2(\theta_{\text{cm}}) \equiv \left\langle \left( \frac{d\sigma^{\text{fit}}}{d\Omega} - \left\langle \frac{d\sigma^{\text{fit}}}{d\Omega} \right\rangle \right)^2 \right\rangle, \quad (3.18)$$

and the systematic error is

$$b_X^2(\theta_{\text{cm}}) \equiv \left( \left\langle \frac{d\sigma^{\text{fit}}}{d\Omega} \right\rangle - \frac{d\sigma^{\text{true}}}{d\Omega} \right)^2. \quad (3.19)$$

The sample mean denoted as  $\langle \dots \rangle$  in Eqs. (3.18) and (3.19) at  $\theta_{\text{cm}}$  is explicitly

$$\left\langle \frac{d\sigma^{\text{fit}}}{d\Omega} \right\rangle \equiv \frac{1}{n} \sum_{i=1}^n \frac{d\sigma_i^{\text{fit}}}{d\Omega}, \quad (3.20)$$

where the number of the pseudo-data set  $n$  is 25.

We define the statistical and systematic errors for the fitted density distributions in the similar way.

$$\sigma_\rho(r)^2 \equiv \left\langle \left( \rho_M^{\text{fit}}(r) - \left\langle \rho_M^{\text{fit}}(r) \right\rangle \right)^2 \right\rangle, \quad (3.21)$$

$$b_\rho(r)^2 \equiv \left( \left\langle \rho_M^{\text{fit}}(r) \right\rangle - \rho_{\text{true}}(r) \right)^2, \quad (3.22)$$

where the sample mean is defined in the same way as in Eq. (3.20).



## 4 Numerical Calculations and Discussions

### 4.1 Completeness Error

We first examine the completeness error, Eq. (3.10), of the Kamimura-Gauss basis functions, taking  $^{58}\text{Ni}$  density as an example. The true density distribution,  $\rho_{\text{true}}(r)$ , is taken to be of the three-parameter Fermi distribution form [54],

$$\rho(r) = \rho_0 \frac{1 + w(r/c)^2}{1 + \exp\{(r - c)/a\}}, \quad (4.1)$$

where  $w = -0.1308$ ,  $c = 4.3092$  [fm], and  $a = 0.5169$  [fm].  $\rho_0$  is the normalization constant determined by

$$\int d\mathbf{r} \rho(\mathbf{r}) = 4\pi \int_0^\infty r^2 dr \rho(r) = A. \quad (4.2)$$

Using Eq. (4.1) above as  $\rho_{\text{true}}(r)$  in Eqs. (3.12) - (3.15), we can determine  $\{\tilde{C}_n\}$ , or  $\tilde{\rho}_M(r)$  from Eq. (3.11), and thus  $\Delta\rho_M^{\text{com}}(r)$  using Eq. (3.10). Our basis functions, the Kamimura-Gauss basis functions, however, depend on the size parameters,  $r_1$  and  $r_M$ , defined in Eq. (3.4). All quantities involved for determining  $\Delta\rho_M^{\text{com}}(r)$ , such as  $\{\tilde{C}_n\}$ , thus also depend on these parameters. We determine the values of  $r_1$  and  $r_M$  for a fixed  $M$ , so as to also minimize

$$\{\rho_{\text{true}}(r) - \tilde{\rho}_M(r)\}^2, \quad (4.3)$$

for the variations of  $r_1$  and  $r_M$ . This minimization is carried out numerically.

Table 1 lists the best-fit values of  $r_1$  and  $r_M$  for different  $M$ , and Fig. 2a) shows the corresponding relative completeness error,  $\Delta\rho_M^{\text{com}}(r)$ . The radial range for the fit is  $R = 10$  [fm]. In this completeness calculation, we impose no normalization condition on  $\tilde{\rho}_M(r)$ , and thus the integrated value of  $\tilde{\rho}_M(r)$  also serves as a measure of goodness of  $\tilde{\rho}_M(r)$ . The integrated value,  $A_M$ , is listed also in Table 1. Note that the exact integrated value is 58 in this case.

Judging from the  $A_M$  value in Table 1 and  $\Delta\rho_M^{\text{com}}(r)$  in Fig. 2a), we see that the appropriate  $M$  would be greater than 10. As we will see in Subsection 4.2, the uncertainty argument gives  $M$  to be about 10. We will choose  $M = 10$  in the rest of this work.

Figure 2a) shows that  $\Delta\rho_M^{\text{com}}(r)$  increases in average as  $r$  increases. For  $M = 10$ ,  $\Delta\rho_M^{\text{com}}(r)$  increases to about 0.01 around 7 [fm] from 0.0001 at the central region. Though the increase is appreciable, it would not be alarming as the density is down by the factor of about 1000 around 7 [fm], compared to the central region of the density. This behavior is quite similar to that of the Fourier-Bessel basis functions (see Appendix C).

We observe that while the  $r_1$  value depends strongly on  $M$ , the  $r_M$  rather weakly. Because of this strong dependence, one may wonder how precisely the size parameters have to be chosen while keeping the completeness error to be reasonably small. In order to address this issue, we choose a fixed set of the size parameters,  $r_1 = 0.5$  [fm] and  $r_M = 6.0$  [fm], which deviate from the best-fit values for all  $M$  shown in Table 1. Figure 2 b) illustrates  $\Delta\rho_M^{\text{com}}(r)$  for this choice of the size parameters. Though  $\Delta\rho_M^{\text{com}}(r)$ 's in this case are larger than those for the best-fit parameter values, we consider  $\Delta\rho_M^{\text{com}}(r)$  in the order of 0.01 to be tolerable.  $A_M$  comes out to be quite close to the exact value, off by 3 [%] even in the worst case of  $M = 5$ .

The mild dependence of the completeness error on the size parameters will be further demonstrated as we apply the same best-fit size parameters for  $^{58}\text{Ni}$  to the case of  $^{78}\text{Ni}$ . As described in Subsection 4.4, we can exploit this mild dependence when we extend the model-independent analysis from the relatively well-known stable nuclei to poorly-known neutron-rich nuclei by keeping the same size parameters.

The Kamimura-Gauss basis functions are not orthogonal among each other. Generally, however, the minimum point of the least-square does not change in the  $M$  dimensional space of the basis functions under a rotation of the space coordinates attached to the basis functions. The minimum point thus remains the same after the Kamimura-Gauss basis functions are orthogonalized by a linear

$M$	$r_1$ [fm]	$r_M$ [fm]	$A_M$
5	0.6	5.8	56.255
10	1.0	5.5	58.030
15	0.7	5.6	57.999
20	0.3	5.7	58.000

Table 1: Dependence of the best-fit parameters of  $r_1$  and  $r_M$  in the Kamimura-Gauss basis functions and of the integrated value of the density  $A_M$  on the number of the basis functions  $M$ . The radial range of the fit is  $R = 10$  [fm].

Group	$B_0$ [mb/str]	$\epsilon_{\min}$ [%]	$\Delta\theta_{\min}$ [mrad]	Rate [sec <sup>-1</sup> ]
A	0.1	2.0	$2 \times 0.3$	$10^3$
B	1.0	3.3	$2 \times 0.3$	$10^2$
C	10.0	6.7	$2 \times 0.3$	10

Table 2: Parameters of the pseudo-data-set group A, B, and C, respectively.  $B_0$  is the magnitude of cross section when the yield count is  $N_0$ .  $N_0 = 10$  in this work.  $\epsilon_{\min}$  [%] is the minimum uncertainty.  $\Delta\theta_{\min}$  [mrad] is the minimum step.

transformation, say, through Schmidt orthogonalization method. Note that this is the case even if a nonlinear transformation were to be used. The error matrix at the minimum point does change, of course, under a transformation, linear or otherwise, by altering the correlated nature of the uncertainties. In the preceding discussions, we have addressed to this issue by performing numerical calculations by artificially moving away from the minimum point. This approach would be more reasonable, as we do not know the true distribution and thus the exact location of the minimum point in practical applications, neither.

Before closing this subsection, we show the dependence of the cross sections on  $M$  in Fig. 3. The Kamimura-Gauss basis functions give satisfactory convergence for  $M \geq 10$ . To go beyond  $20^\circ$  it gives nice diffraction patterns, especially for  $M \geq 15$ . The solid curve ( $M = 20$ ) is on another dotted curve which is drawn by using the original  $\rho_{\text{true}}(r)$  for  $\theta_{\text{cm}} < 20^\circ$ , and slightly differs for  $\theta_{\text{cm}} > 20^\circ$ . This behavior is better than that of the Fourier-Bessel basis functions. (see Appendix C).

## 4.2 Pseudo Data

As we described in Subsection 3.2, we generate 25 pseudo data at each scattering angle. The values of the pseudo data change when the yield parameter  $B_0$  is changed. We carry out our analysis for three different values of  $B_0 = 0.1, 1.0, \text{ and } 10$  [mb/str]. Each value of  $B_0$  [mb/str] provides different sets of the pseudo data, each set consisting of 25 data at each scattering angle. We denote the set for  $B_0 = 0.1$  [mb/str] to be the pseudo-data-set group A, the set for  $B_0 = 1.0$  [mb/str] to be the group B, and the set for  $B_0 = 10.0$  [mb/str] to be the group C. We take the minimum uncertainty  $\epsilon_{\min} = 2.0, 3.3, \text{ and } 6.7$  [%] for pseudo-data-set group A, B and C, respectively (Table 2). The definitions of these quantities are given in Appendix D.

As an example, we plot a pseudo-data set of the pseudo-data-set group A in Fig. 4. The solid curve is the same as in Fig. 1. The kinematical conditions are:

$$\theta_{\max} \leq 25^\circ \quad \Leftrightarrow \quad q_{\max} \leq 750[\text{MeV}]. \quad (4.4)$$

$$\Delta\theta \simeq 1.0^\circ \quad \Leftrightarrow \quad \Delta q \simeq 20[\text{MeV}], \quad (4.5)$$

where  $\Delta q$  is an increment in momentum transfer. Since we take a step in  $\theta$  smaller than  $1^\circ$  in the forward direction,  $\Delta q$  can be smaller.

Some of the parameters of the expansion of the density distribution are related to the kinematical conditions of the experiment [13, 18, 55, 56]. The followings are the rough estimates for them:  $r_{\max}$  is the maximum distance to probe by the experiment, and  $r_{\max} \simeq \pi/\Delta q \simeq 30$  [fm]. We take  $R$

= 10 [fm] ( $\leq r_{\max}$ ). Since we are interested in the surface region, not in the tail, this value of  $R$  is enough to cover the region. This choice is consistent with the charge density distribution studies for the medium-heavy nuclei,  $^{50,52,54}\text{Cr}$  [57]. The resolution of the fitted density distribution is  $\Delta r = \pi/q_{\max} \simeq 0.85$  [fm]. The dimension of the model space is  $M \simeq q_{\max}R/\pi$ . We estimate  $M = 10 \sim 15$ .

In order to make our discussions more realistic, we compare different pseudo-data-set groups with experimental setups expected at the RIBF. We first introduce two quantities, the counting rate,  $J(\theta_\alpha)$  [ $\text{sec}^{-1}$ ], and the time for measurements,  $T$  [sec]. The multiplication of the two gives the yield count,

$$N_{\text{yield}}(\theta_\alpha) = J(\theta_\alpha) T \quad (4.6)$$

in Eq. (3.7).  $J(\theta_\alpha)$  is expressed as

$$J(\theta_\alpha) = N_{\text{tar}} j_{\text{beam}} \frac{d\sigma_\alpha^{\text{true}}}{d\Omega} \Delta\Omega, \quad (4.7)$$

where  $N_{\text{tar}}$  is the number of the particles in the reaction region of the target,  $j_{\text{beam}}$  [ $\text{cm}^{-2} \text{sec}^{-1}$ ] is the current of incident particles.  $d\sigma_\alpha^{\text{true}}/d\Omega$  [ $\text{cm}^2 \text{str}^{-1}$ ] is the cross section at  $\theta_\alpha$ , and  $\Delta\Omega$  [str] is the solid angle covered by the detector.

At the RIBF, experiments of proton-nucleus elastic scattering are performed in the inverse kinematics that the incident nuclear beam collides with protons in the target in the laboratory frame. Consider a  $\text{CH}_2$  target with the thickness of 10 [ $\text{mg cm}^{-2}$ ]. In terms of the Avogadro number  $N_A = 6.03 \times 10^{23}$  [ $\text{mol}^{-1}$ ], the number of the protons in the target is  $N_{\text{tar}} = 2 \times N_A \times (10 \times 10^{-3}/14) = 2 \times 0.43 \times 10^{21}$  [ $\text{cm}^{-2}$ ]. Let us assume the radius of the incident beam to be 1 [cm] and the number of the detectors to be 10 covering 50 [mstr] each (that is,  $\Delta\Omega = 0.5$  [str]), and also take  $d\sigma_\alpha^{\text{true}}/d\Omega = 0.1$  [mb/str], and the rate of particle production to be  $10^3$  [ $\text{sec}^{-1}$ ] (that is,  $j_{\text{beam}} = 10^3/\pi$  [ $\text{cm}^{-2} \text{sec}^{-1}$ ]).  $J(\theta_\alpha)$  is then in this case

$$\begin{aligned} J(\theta_\alpha) &= \pi [\text{cm}^2] \times 2 \times 0.43 \times 10^{21} [\text{cm}^{-2}] \times \frac{10^3}{\pi} [\text{cm}^{-2}\text{sec}^{-1}] \\ &\quad \times 10^{-28} [\text{cm}^2\text{str}^{-1}] \times 0.5 [\text{str}] \\ &= 4.3 \times 10^{-5} [\text{sec}^{-1}]. \end{aligned} \quad (4.8)$$

If we suppose 1-week measurement, *i.e.*,  $T = 6.048 \times 10^5$  [sec], we have  $N_{\text{yield}}(\theta_\alpha) = 26.0$ , or in the order of 10 counts. Therefore, 0.1 [mb/str] roughly corresponds to a 10 yield for the above conditions, which is pseudo-data-set group A. The correspondence of the rate of particle production to various pseudo-data-set groups is summarized in the Table 2.

Note that the expected production rate of  $^{70}\text{Ni}$  at the RIBF is about  $10^3$  [ $\text{sec}^{-1}$ ], while that of  $^{78}\text{Ni}$  is about 10 [ $\text{sec}^{-1}$ ]. The former corresponds to the pseudo-data-set group A and the latter to the group C. These correspondences are still valid if the target thickness becomes 5 [ $\text{mg cm}^{-2}$ ], because we have estimated them by considering  $N_{\text{yield}}(\theta_\alpha) = 26.0$  to be the order of 10 counts.

### 4.3 Least-Square fitting

For the three pseudo-data-set groups of proton- $^{58}\text{Ni}$  elastic scattering generated in the previous subsection, we perform least-square fittings of Eq. (3.3) in Subsection 3.1 to obtain the density distributions,  $\rho(r)$ . In the fittings, the normalization of  $\rho(r)$  is treated as one of the pseudo data with an uncertainty of about 0.2 [%], far smaller than the uncertainties assigned to the other pseudo data. Note that the normalization of the basis functions is automatically taken care of in this way, because such a high precision datum works as a constraint. The numerical minimization is done by the use of MINUIT [51].

There is another usage of the normalization. Without putting a high precision number to the normalization, one may make the fitting first, and calculate the normalization after the fitting is completed. This normalization should fluctuate around the true number, and the degree of this fluctuation could work as a measure of the goodness of the fitting. We do not take this way, because we are interested in the statistical and systematic errors of the density distribution for the fixed normalization.

The numerical results for the pseudo-data-set group A, B, and C are shown in Figs. 5, 6, and 7, respectively, for  $R = 10$  [fm] and  $M = 10$ . As the particle production rate decreases from Fig. 5 to Fig. 7 (see Table 2), quality of the pseudo data becomes worse accordingly. Each figure consists of a) 25 fitted cross sections (shown with solid curves) with all pseudo data (crosses with bars), and b) 25 fitted density distributions, (solid curves), with the original density distribution (the dotted curve). The density distributions are shown for  $r^2 \rho_M^{\text{fit}}(r)$  including the radial phase space of  $r^2$ . It is this form that the data actually constrain. In the figures we show the statistical and systematic errors divided by the true density distributions. One can see that the relative uncertainties of the fitted density around the true density itself without  $r^2$  from those figures. The average values of the least square divided by the number of degrees of freedom,  $\chi^2/\text{DOF}$ , and of the RMS radius,  $\langle r^2 \rangle^{1/2}$ , obtained from the 25 different pseudo-data sets are also shown in the figures. The number of DOF is ( $\equiv N_{\text{data}} - M$ ).

For all pseudo-data-set groups, the density distributions,  $r^2 \rho_M^{\text{fit}}(r)$ , have larger uncertainties in the central region than in the surface region. This result is in agreement with the previous works [38, 39, 40, 41, 42], and is analogous to what was found in the determination of charge density distributions (for example, [9, 18]). The original distribution drawn by the dotted curve is included in the error-band, which signifies that our procedure consistently provide probable density distributions within the uncertainty. Even with a pseudo-data-set group of lower yields, it seems that the surface has smaller uncertainty than the center. It is reasonable that the surface region of  $\rho_M^{\text{fit}}(r)$  is determined, because the cross section carries the information of this region [34].

In each case,  $\chi^2/\text{DOF}$  is about unity. For the pseudo-data-set group B we have checked that the least square,  $\chi^2$ , of each pseudo data set distributes according to the  $\chi^2$ -distribution (Appendix E). This confirms that our numerical simulations make sense statistically. The  $\langle r^2 \rangle^{1/2}$  of each pseudo-data-set group has less than 2 % uncertainty, including the original value of 3.764 [fm].

Comparing Figs. 5, 6, and 7, we find that while the differential cross sections fluctuate for  $\theta_{\text{cm}} > 20^\circ$ , the nuclear densities fluctuate for  $r < 2$ [fm], and that the fluctuations become more appreciable again as the quality of the pseudo data decreases. Note that when the number of terms of the Kamimura-Gauss basis functions,  $M$ , is increased, the  $\chi^2/\text{DOF}$  becomes closer to unity but the fluctuations increase, as similar observation was made previously [13, 55, 56].

In order to see explicitly the role of large  $\theta_{\text{cm}}$  or large- $q$  pseudo data, we remove the pseudo data of  $\theta_{\text{cm}} > 15^\circ$  from the pseudo-data-set group C, and call the truncated data set to be the group C'. Figures 8 a) and b) show that the fluctuations by the pseudo-data-set group C' are greater than those by the group C both in the cross sections and in the density. Note that the mean value and the variance of  $\langle r^2 \rangle^{1/2}$  changes much less, because the density in the surface region mainly affects  $\langle r^2 \rangle^{1/2}$ .

The statistical uncertainty and the systematic error are examined in Figs. 9 and 10. We see that as the quality of the pseudo data decreases, the statistical uncertainty tends to increase but the systematic error does less. Furthermore, Fig. 9 shows that both of the uncertainty and the error in the surface region of our interest,  $r = 3 \sim 5$  [fm], are smaller than in the other regions, which is in consistent with the previous works [40, 41]. This is one of our major results.

The quantities examined here are the relative quantities. One should not be alarmed with the somewhat large values for  $r > 6$  [fm], because they are associated with quite small values of the density. A similar caution is needed with the cusps appearing in Fig. 10, because they are associated with the dips in the cross sections. The cusps are expected to reduced once the Coulomb interaction is included in the analysis.

#### 4.4 Neutron-rich nuclei

We now examine an extension of our analysis to the case of neutron-rich nuclei by taking the case of the proton- $^{78}\text{Ni}$  elastic scattering as an example. Here, we use the pseudo-data-set group C to generate its pseudo data, as the expected particle production rate of  $^{78}\text{Ni}$  at the RIBF, 10 [ $\text{sec}^{-1}$ ], corresponds to the case of the group C. As the true density, we take the vector part of the relativistic mean-field density [58]. Figure 11a) shows the true density distribution of  $^{78}\text{Ni}$  together with the distribution fitted by the use of fifteen ( $M = 15$ ) Kamimura-Gauss basis functions. They agree each other quite closely, as they could not be identified separately by eye.  $\langle r^2 \rangle^{1/2} = 4.181$  [fm] is obtained

from these density distributions.

We use the same size parameters,  $r_1 = 0.7$  [fm], and  $r_M = 5.6$  [fm], as those that we used for  $^{58}\text{Ni}$  with  $M = 15$  (Table 1). The completeness errors for  $M = 10$  and  $15$  are shown in Fig. 11 b), which are very close to those for  $^{58}\text{Ni}$ . Therefore, once we determine the size parameters for a given  $M$  for a known density distribution, such as that for stable nuclei, we could safely use them for the isotopes of the nucleus.

The numerical results of the least square fittings are shown in Fig. 12 a) and b). We use  $R = 10$  [fm] and  $M = 10$ . The size parameters,  $r_1 = 1.0$  [fm], and  $r_M = 5.5$  [fm], are the same values as those of  $^{58}\text{Ni}$  (Table 1). The pseudo data are fitted well, especially in the forward direction, as seen in Fig. 12 a). Figure 12 b) shows that the fitted density distributions fluctuate in the central region, but are stable in the surface region. Unfortunately,  $\langle r^2 \rangle^{1/2}$  obtained from the fittings is slightly smaller than that of the true distribution shown in Fig. 11 a), but within the fluctuation.

Similarly to the discussions in the previous subsection, we also show the statistical uncertainty and the systematic error in Figs. 13 and 14. Figure 13 confirms that the density distribution for this neutron-rich nucleus can be determined well in the surface region, which is consistent with the result obtained by using the Fourier-Bessel basis functions (Fig. 15).  $M = 7$  is the best choice for this pseudo-data-set group for the Fourier-Bessel basis functions of  $R = 10$  [fm].

One should be careful for the statistical uncertainty in the central region. By comparing Fig. 13 with Fig. 15, one can see that the statistical uncertainty of the Kamimura-Gauss basis functions in the central region fluctuates much larger, about an order of magnitude, than the Fourier-Bessel ones. As we mentioned in Introduction, since the statistical uncertainty should carry the information only on the quality of data, any basis function has to show the statistical uncertainty distribution of similar quality for the same data. The error estimation of the Kamimura-Gauss basis functions in the central region should be treated with caution.

The behavior of these uncertainty and error is similar to that for the stable nucleus examined in the previous subsection. We thus expect that the surface region of nuclei could be better determined than the central region for relatively low intensity beam.

Before closing this section, we should add a comment. To discuss how the density distributions or the radii change in the isotope chain, the difference between the one from the neighboring nucleus is a good measure, because the model dependence could be canceled by the subtraction procedure [35, 59]. In this work we are interested in how precisely we can determine the density distribution itself of the neutron-rich nuclei with low intensity beam. We leave the problem concerning the discussion on such differences for our future work.

## 5 Summary and Discussion

The matter density distribution in the surface region is shown to be determined well by a relatively low intensity beam in the order of  $10 \text{ [sec}^{-1}\text{]}$ , which is an expected intensity of the  $^{78}\text{Ni}$  beam at the RIBF of RIKEN.

We have demonstrated how the determination of the density distributions becomes poorer, especially in the central region, as the quality of data becomes worse. The demonstration is made through a simulation by the use of three pseudo-data-set groups of proton-nucleus elastic scattering, corresponding to beam intensities expected to be available at the RIBF. Our discussion here is qualitatively in accord with what has been found in electron scatterings [9, 10, 11, 12, 13, 18], and also with what has been done in proton scatterings [40, 41].

The matter density distribution of neutron-rich nuclei is determined by fixing the parameters in the basis functions to those of the neighboring stable nucleus. This procedure is expected to be a practical way of treating neutron-rich nuclei, as the beam intensities of neutron-rich nuclei tend to be less and the determination of their matter density distributions will be poorer. We have demonstrated this procedure to be feasible by taking  $^{78}\text{Ni}$  as an example.

In this work, we have focused on the question, how well the nuclear density distribution is determined from experimental data with the quality expected at the upcoming facilities, *assuming* that the proton-nucleus potential is known with no uncertainty. The uncertainty for this must be included in the practical evaluation of the uncertainty in the determination of the matter density distribution. The question of the potential will require a close examination beyond the use of  $t$ - $\rho$  form, especially as the incident energy becomes lower. Also, a special attention may have to be given to neutron-rich nuclei [60].

We expect that the uncertainty associated with the use of the eikonal form instead of the partial wave decomposition is small, though the absolute magnitude itself could be substantial. In order to clarify this and the uncertainty associated with the potential, they will be the issues that we wish to address in future work.

### Acknowledgements

We acknowledge I.Tanihata for his invaluable suggestions and comments, and M. Kamimura and K.Yazaki for stimulating discussions. We thank T.Ohnishi, and T.Suda, and K.Katori for their assistance on our generation of the pseudo data to be realistic to the RIBF facilities. G.D.Alkhazov and A.Lobodenko informed us of their work [33], and M.Oka provided us a computer code for orthogonalization of a function set. This work is supported under the Special Postdoctoral Research Program at RIKEN and by the U.S. DOE at CSUN (DE-FG03-87ER40347) and the U.S. NSF at Caltech (PHY00-71856 and PHY97-22428).

## APPENDIX

### A Kamimura-Gauss Basis functions

Here we summarize the formulae associated with the Kamimura-Gauss basis functions, which have been used by Kamimura [21] in various applications, for example, in few-body calculations [61].

The basis functions are expressed as

$$f_n(r) = \exp(-r^2/r_n^2) \theta(R - r), \quad (n = 1, \dots, M), \quad (\text{A.1})$$

where the size parameter,  $r_n$ , is determined through a geometrical progression,  $r_n = r_1 a^{n-1}$  ( $n = 1, \dots, M$ ).  $\theta(x)$  is the step function, and  $R$  is a scale parameter constrained by the kinematical condition [13]. Note that the standard version of the Kamimura-Gauss basis functions has no restriction of  $r_M < R$  [21].

The inner product of two basis functions is defined by

$$(f_n, f_{n+m})_l \equiv 4\pi \int_0^\infty r^l dr f_n(r) f_{n+m}(r) \quad (\text{A.2})$$

$$= \frac{2\pi}{\alpha_{n,m}^{(l+1)/2}} \{ \Gamma((l+1)/2) - \Gamma((l+1)/2, \alpha_{n,m} R^2) \}, \quad (\text{A.3})$$

where

$$\alpha_{n,m} \equiv \frac{1}{r_n^2} + \frac{1}{r_{n+m}^2} = \frac{1}{r_n^2} \left( 1 + \frac{1}{a^{2m}} \right), \quad (\text{A.4})$$

and  $l$  is the power of the phase volume and is set to be a non-negative integer.  $\Gamma(z)$  ( $= \Gamma(z, 0)$ ) is the Gamma function, and  $\Gamma(z, p)$  is the incomplete Gamma function of the second kind.

When the normalization is suitably chosen, the expression of the inner product becomes simple. If  $(\tilde{f}_n, \tilde{f}_n)_{l=2} = 1$  for  $\tilde{f}_n(r) = N_n f_n(r)$ , we obtain

$$\frac{1}{N_n^2} = \frac{\pi}{\sqrt{2}} r_n^3 (\Gamma(3/2) - \Gamma(3/2, 2R^2/r_n^2)). \quad (\text{A.5})$$

Note that when  $R \rightarrow \infty$ , the expressions become greatly simplified:

$$\frac{1}{N_n^2} = \frac{\pi^{3/2}}{2\sqrt{2}} r_n^3, \quad (\text{A.6})$$

and

$$(\tilde{f}_n, \widetilde{f_{n+m}})_{l=2} = \frac{2\sqrt{2} a^{3m/2}}{(1 + a^{2m})^{3/2}}. \quad (\text{A.7})$$

The basis functions have the following properties: 1) They are not orthogonal, but are linearly independent. One can easily verify the linear independence by demonstrating the Wronskian, to be non-zero except at the infinity. 2) The derivative with respect to  $r$  vanishes at  $r = 0$ , and thus the derivative of the density expanded in terms of the basis functions is also zero at  $r = 0$ . Note that this property is the same as that of the Gaussian basis functions used by Sick [24]. 3) The coefficients of the Kamimura-Gauss basis functions can be negative, while Sick restricted the coefficients of his Gaussian basis functions to be positive [24]. Actually, the coefficients in our case tend to appear almost equally in both signs. 4) The set of the Kamimura-Gauss basis functions does not form a complete set, even if the infinite number of terms are used. Note that a finite number of terms is always used in practice, and the issue of completeness is an academic question. 5) They depend on two parameters, such as  $r_1$  and  $r_M$ .

In our application, we choose  $r_1$  and  $r_M$  by minimizing  $D(\tilde{C}_n)$  of Eq. (A.9) below. Though  $r_1$  depends strongly on  $M$ , it is found to vary little for different isotopes. The expansion coefficients for the normalized basis functions,  $\tilde{C}_n$ , are determined by minimizing

$$D(\tilde{C}_n) \equiv |\rho_{\text{true}}(r) - \rho_M^{\text{fit}}(r)|^2 \quad (\text{A.8})$$

$$= |\rho_{\text{true}}(r) - \sum_{n=1}^M \tilde{C}_n \tilde{f}_n(r)|^2, \quad (\text{A.9})$$

that is, by satisfying  $\partial D(\tilde{C}_m)/\partial \tilde{C}_m = 0$ . This condition leads to

$$\tilde{f}_m(r) \rho_{\text{true}}(r) = \left( \sum_{n=1}^M \tilde{C}_n \tilde{f}_n(r) \right) \tilde{f}_m(r), \quad (n, m = 1, \dots, M). \quad (\text{A.10})$$

We thus obtain

$$\sum_{m=1}^M F_{n,m} \tilde{C}_m = v_n, \quad (\text{A.11})$$

where

$$F_{n,m} \equiv 4\pi \int_0^\infty r^l dr \tilde{f}_n(r) \tilde{f}_m(r). \quad (\text{A.12})$$

$$v_n \equiv 4\pi \int_0^\infty r^l dr \tilde{f}_n(r) \rho_{\text{true}}(r). \quad (\text{A.13})$$

Note that one can also follow the same procedure in the case of the coefficients,  $\tilde{C}_n$ , for non-normalized basis functions. The phase-volume parameter,  $l$ , is chosen by depending on how much weight one wishes to impose on the out-region. In the present analysis, we choose  $l = 0$  in order to include the information of the whole region equally.

Finally, Eq. (A.11) is inverted numerically to yield

$$\tilde{C}_m = \sum_{n=1}^M F_{m,n}^{-1} v_n. \quad (\text{A.14})$$



## B Eikonal Expressions

For the purpose of completeness and clarification, we summarize the eikonal expressions [17], which we have used.

The differential cross section of the proton-nucleus elastic scattering in the center-of-mass frame is expressed as

$$\frac{d\sigma_{\text{el}}}{d\Omega} = F_{\text{kin}} |T(\mathbf{q})|^2 \quad (\text{B.1})$$

with the kinematical factor  $F_{\text{kin}} = |\mathbf{p}|^2/(2\pi)^2$ .  $\mathbf{q}$  ( $= \mathbf{p} - \mathbf{p}'$ ) is the three-momentum transfer, where  $\mathbf{p}$  and  $\mathbf{p}'$  are the momenta of the incident and of the outgoing proton, respectively.  $T(\mathbf{q})$  is the  $t$ -matrix expressed in the eikonal form,

$$T(\mathbf{q}) = \int d\mathbf{b} \exp\{i\mathbf{q} \cdot \mathbf{b}\} (1 - \exp\{i\chi(\mathbf{b})\}), \quad (\text{B.2})$$

$$= 2\pi \int_0^\infty b db J_0(qb) (1 - \exp\{i\chi(b)\}), \quad (\text{B.3})$$

where  $J_0(qb)$  is the zero-th order Bessel function. The profile function,  $\chi(\mathbf{b})$ , is given by

$$\chi(\mathbf{b}) = \frac{2\pi}{|\mathbf{p}|} f(\mathbf{0}) \int_{-\infty}^\infty dz' \rho(\mathbf{b}, z'), \quad (\text{B.4})$$

where  $\rho(\mathbf{r})$  is the one-body matter density distribution, and  $\mathbf{r} = (\mathbf{b}, z)$ .  $\mathbf{b}$  is the impact parameter vector,  $\mathbf{b} \perp \mathbf{p}$ , and the integration in  $z$  is taken in the direction of the incident momentum,  $\mathbf{p}$ .  $f(\mathbf{0})$  is the nucleon-nucleon scattering amplitude in the forward direction,  $\mathbf{q} = \mathbf{0}$ .

$$f(\mathbf{0}) = \frac{|\mathbf{p}|}{4\pi} (i + \alpha) \sigma_{\text{NN}}^{\text{total}}. \quad (\text{B.5})$$

The expression of  $\chi(\mathbf{b})$  above corresponds to the first-order optical potential in the Glauber approximation. The Coulomb interaction is not included here, but could be included straightforwardly [17, 52].

For the numerical calculation of Fig. 1, we use the parameters of Eq. (B.5) as follows [62]:

$$|\mathbf{p}_{\text{lab}}| = \sqrt{(K + m)^2 - m^2} = 1.75 \text{ [GeV}/c]. \quad (\text{B.6})$$

$$\alpha = -0.0687, \quad \sigma_{\text{NN}}^{\text{total}} = 43.1 \text{ [mb]}, \quad (\text{B.7})$$

where  $m$  is the nucleon mass, and  $K$  is the kinetic energy of the incident proton, which is  $K = 1.047$  [GeV]. We use these parameters for all the numerical calculations in this work.

We calculate the cross section of proton- $^{58}\text{Ni}$  elastic scattering as an example in Subsection 3.1 and Section 4. We take the three-parameter Fermi distribution, Eq. (4.1), for the matter density distribution of  $^{58}\text{Ni}$  to create the pseudo data in Subsection 4.2, because the experimental data of differential cross sections of electron-nucleus elastic scattering for various nuclei are fitted well with this form, including  $^{58}\text{Ni}$  [54], and because the matter density distribution of  $^{58}\text{Ni}$  is considered to be quite similar to the charge density distribution. Actually, the experimental data of differential cross section of proton- $^{58}\text{Ni}$  elastic scattering are fitted well with this form [31].

One should be careful for large- $r$  behavior of the three-parameter Fermi distribution, Eq. (4.1), because it becomes negative for  $r > r_c$  if  $w$  is negative. That is,  $\rho(r_c) = 0 \Leftrightarrow 1 + w(r_c/c)^2 = 0$ , for  $r_c = c/\sqrt{-w}$ . For our choice of the parameters,  $r_c = 11.915$  [fm]. We put  $\rho(r) = 0$  for  $r > r_c$ .

With the fitted density distribution,  $\rho_M^{\text{fit}}(r)$ , of Eq. (3.1) in terms of the Kamimura-Gauss basis functions defined by Eq. (3.4), we can perform the integration of the profile function in Eq. (B.4) analytically due to the nature of the Gaussian functions:

$$\begin{aligned} \chi(\mathbf{b}) &= \frac{2\pi}{|\mathbf{p}|} f(\mathbf{0}) \sum_{n=1}^M C_n r_n \exp\{-\mathbf{b}^2/r_n^2\} \\ &\quad \times \{\Gamma(1/2) - \Gamma(1/2, (z_{\text{max}}/r_n)^2)\}, \end{aligned} \quad (\text{B.8})$$

where  $\Gamma(1/2) = \sqrt{\pi}$ , and  $z_{\max}^2 = R^2 - \mathbf{b}^2$ .  $\Gamma(z, p)$  is the incomplete Gamma function of the second kind. This integration reduces our numerical task for the cross sections, and brings us the numerically stable results.

$R = 10$ [fm]	
$M$	$A_M$
5	58.115
10	57.974
15	58.001
20	57.999

Table 3: Dependence of the integrated value of the density  $A_M$  of the Fourier-Bessel basis functions on the number of the basis functions  $M$ . The radial range of the fit is  $R = 10$  [fm].

## C Fourier-Bessel Basis Functions

Here we summarize some formulae concerning the Fourier-Bessel basis functions, and show its completeness error introduced in Subsection 3.3.1. The Fourier-Bessel basis functions are defined by [13]

$$f_n(r) = j_0(n\pi r/R) \theta(R - r), \quad (\text{C.1})$$

where  $j_0(x)$  is the 0-th order spherical Bessel function, which is expressed by  $j_0(x) = \sin x/x$ .  $R$  is a scale parameter determined by the discussion under eq. (4.5).  $\theta(x)$  is the step function.

If we define the inner product as

$$(\tilde{f}_n, \tilde{f}_m)_{l=2} \equiv 4\pi \int_0^\infty r^2 dr \tilde{f}_n(r) \tilde{f}_m(r), \quad (\text{C.2})$$

we obtain the normalized version of this basis function as,

$$\tilde{f}_n(r) = N_n f_n(r), \quad (\text{C.3})$$

where  $N_n = \sqrt{n^2\pi/(2R^3)}$ .

Since the Fourier-Bessel basis functions are orthogonal to each other, *i.e.*,  $(\tilde{f}_n, \tilde{f}_m) = \delta_{n,m}$ . we can easily obtain  $\tilde{C}_n$  by the following equation:

$$\tilde{C}_n = 4\pi \int_0^\infty r^2 dr \tilde{f}_n(r) \rho_{\text{true}}(r). \quad (\text{C.4})$$

As in Subsection 4.1, we show the numerical results of  $\Delta\rho_M^{\text{com}}(r)$ , defined by Eq. (3.10), for the Fourier-Bessel basis functions of  $R = 10$  [fm] with the number of terms,  $M$ , being 5, 10, 15, and 20, in Fig. 16 a). This figure corresponds to Fig. 2 a). Here we also systematically determine the expansion coefficients of the Fourier-Bessel basis functions,  $\tilde{C}_n$ , of Eq. (C.4). Roughly speaking, the magnitude of the coefficients becomes smaller as  $n$  increases, because the overlap of  $\tilde{f}_n(r)$  with  $\rho_{\text{true}}(r)$  becomes smaller due to the oscillatory nature of the basis functions as one can see from Eq. (C.4).

Although each term of the Fourier-Bessel basis functions and the Kamimura-Gauss ones shows different behavior in  $r$ , it is interesting to see that  $\Delta\rho_M^{\text{com}}(r)$  of the both bases show similar oscillating patterns in  $r$ . The convergence at each point becomes better as  $M$  increases for the both cases, and the convergence for the Fourier-Bessel basis functions become better beyond  $M = 15$  in contrast to the Kamimura-Gauss ones. Up to  $M = 15$ , the both bases have almost the same quality of convergence. The uncertainties for  $M \geq 10$  are the order of  $10^{-2}$  or less, and for  $M \geq 15$  are the order of  $10^{-3}$  or less in the region of  $1 \text{ [fm]} \leq r \leq 5 \text{ [fm]}$ , which covers the surface region of nuclei. The uncertainty becomes worse in the region of  $r > 5 \text{ [fm]}$ , but it is still the order of  $10^{-2}$ .

As in the completeness calculation in Subsection 4.1, we impose no normalization condition (3.2) on  $\tilde{\rho}_M(r)$ , Eq. (3.11), here, and thus the integrated value of  $\tilde{\rho}_M(r)$  also serves as a measure of goodness of  $\tilde{\rho}_M(r)$ . As in Table 1 in Subsection 4.1, Table 3 lists the integrated value,  $A_M$ . Note that the exact integrated value is 58 in this case, too. As one can see from this table,  $A_M$  stays in about 0.2 %-fluctuation for all  $M$ . They are all tolerable. For  $M$  larger than 5,  $A_M$  can be determined within the error of 0.05 %.

Finally, we show the numerical results of the corresponding cross sections for each  $M$  in Fig. 16 b). This figure corresponds to Fig. 3. The Fourier-Bessel basis functions give satisfactory convergence for  $M \geq 10$ , similar to the Kamimura-Gauss ones, and, if we restrict ourselves to see  $\theta < 10^\circ$ , we already obtain good convergence even for  $M = 5$ . The solid curve ( $M = 20$ ) is almost on the dotted curve (drawn by the original  $\rho_{\text{true}}(r)$ ) for  $\theta_{\text{cm}} < 20^\circ$ , but unfortunately the diffraction pattern is broken for  $\theta_{\text{cm}} > 20^\circ$ . The other curves,  $M < 20$ , are also differs from the dotted curve in this large-angle region.

Such broken patterns of the Fourier-Bessel basis functions could be numerical artifacts coming from the numerical integration, which is almost inevitable for numerical fittings, while they do not appear for the Kamimura-Gauss basis functions. Thus, when we apply the Fourier-Bessel basis functions to those fittings, we should be careful for cross sections of the large scattering angle. They most probably affect the central region of the density distributions. For  $\theta < 20^\circ$  and  $M \geq 10$ , both the Fourier-Bessel and Kamimura-Gauss basis functions give good convergence.

## D Small Scattering Angles

Here we explain how to reduce the separation of pseudo data in  $\theta_\alpha$  from  $1.0^\circ$  near the forward direction. The prescription to create pseudo data is written in Subsection 3.2. To make the way to shrink the step of pseudo data systematic, we define the minimum uncertainty,  $\epsilon_{\min}$ . Since we are to assign a statistical uncertainty more than this, we restrict  $\epsilon_{\min}^2 \leq 1/N_{\text{PD}}(\theta_\alpha)$  at each data point, where  $N_{\text{PD}}(\theta_\alpha)$  is the yield count of the pseudo data at  $\theta_\alpha$ , defined in the same way as in Eq. (3.8). We obtain  $\Delta\theta_\alpha$  by keeping

$$\Delta\theta_0 \frac{1}{\epsilon_{\min}^2} \simeq \Delta\theta_\alpha N_{\text{PD}}(\theta_\alpha). \quad (\text{D.1})$$

In the region where the theoretical cross section changes drastically this formula overestimates or underestimates the step.

For large  $N_{\text{PD}}(\theta_\alpha)$ ,  $\Delta\theta_\alpha$  becomes smaller than a bin of the detector. In order to avoid such an unrealistic estimate, we define the minimum step,  $\Delta\theta_{\min}$ , and make  $\Delta\theta_\alpha$  not less than that. The minimum step is expected to be 0.3 [mrad] ( $= 17.2^\circ \times 10^{-3}$ ) in the proton-fixed frame at the RIBF. Since our cross sections are calculated in the center-of-mass frame, we are careful for the inverse kinematics of the RIBF. We take  $\Delta\theta_{\min} = 2 \times 0.3$  [mrad], which is safe if we transform  $\Delta\theta_{\min}$  in the proton-fixed frame to the center-of-mass frame. The requirement to identify a proton-nucleus elastic scattering makes the minimum step very small. In the forward direction  $\theta$  can be determined precisely at the RIBF. Although the data have some uncertainty in  $\theta$  in the large  $\theta_{\text{cm}}$  region, we neglect it in this work.

## E Distribution of the Fitted Results

According to the statistics, the least square,  $\chi^2$ , of Eq. (3.3) is known to obey the  $\chi^2$ -distribution defined by

$$f_\nu(\chi^2) = \begin{cases} 2^{-\nu/2}\Gamma(\nu/2)^{-1} (\chi^2)^{\nu/2-1} \exp(-\chi^2/2), & (\chi^2 > 0), \\ 0, & (\chi^2 < 0), \end{cases}$$

where  $\nu (> 0)$  is the degree of freedom, provided that each term consisting the least square of Eq. (3.3),  $(d\sigma_\alpha^{\text{data}}/d\Omega - d\sigma_\alpha^{\text{true}}/d\Omega) / \epsilon_\alpha$ , obeys the standard normal distribution [14].

We use this fact to examine the consistency of our simulation by calculating the following quantity.

$$F_\nu(\chi^2) = \int_0^{\chi^2} dv f_\nu(v). \tag{E.1}$$

We compare it with our numerical results in Table 4.

We take the pseudo-data-set group B as an example. The number of data points of each pseudo-data set is 40, 41, and 42. Such a fluctuation of the number of data point occurs, because some pseudo data are rejected from the pseudo-data set when they become less than  $10^{-2}$  [mb/str]. We use the pseudo-data sets of 41 data points, because this is the largest portion of the group. The degree of freedom becomes 31, as  $M = 10$ . The case contains 15 pseudo-data sets out of 25.

Table 4 shows that our fitted results distribute consistently with the calculated  $\chi^2$ -distribution, and that our simulations are in accord with statistical considerations.

$\chi_a^2$	$F(\chi_a^2)$ calc.	$F(\chi_a^2)$ PDSG-B
20	0.064	0.067 (= 1/15)
30	0.48	0.33 (= 5/15)
40	0.87	0.87 (= 13/15)
50	0.98	1.00 (= 15/15)

Table 4: Comparison of calculated values of integrated  $\chi^2$  distribution with the corresponding quantity of the pseudo-data-set group B. The degree of freedom is 31. The bracket in the right most column shows the fraction which satisfies the condition.

## References

- [1] Y.Yano, T.Katayama, A.Goto, and M.Kase, *AIP Conf. Proc.*, **576**, (2001) 679.
- [2] White Paper “Scientific Opportunities with an Advanced ISOL Facility”, Nov., 1997.  
<http://srf.srv.jlab.org/isol/>
- [3] A.N.Antonov, P.E.Hodgson, and I.Zh.Petkov,  
*Nucleon Momentum and Density Distributions in Nuclei*,  
Clarendon Press, 1988.
- [4] I.Tanihata *et al.*, *Phys. Lett.*, **B160**, (1985) 380;  
*Phys. Rev. Lett.*, **55**, (1985) 2676.
- [5] Proceedings of International Symposium on *Structure and Reactions of Unstable Nuclei*,  
ed. K.Ikeda and Y.Suzuki, World Scientific, Singapore, (1991).
- [6] C.A.Bertulani, L.F.Canto, and M.S.Hussein, *Phys. Rep.*, **226**, (1993) 281.
- [7] I.Tanihata, *J. Phys.*, **G22**, (1996) 157.
- [8] L.R.B.Elton, *Nuclear Sizes*, Oxford, (1961).
- [9] D.Berdichevsky and U.Mosel, *Nucl.Phys.*, **A388**, (1982) 205.
- [10] C.J.Batty, E.Friedman, H.J.Gils, and H.Rebel,  
*Adv. Nucl. Phys.*, **Vol.19**, (1989) 1.
- [11] I.Sick, *Lecture Notes in Physics*, **236**, (1985) 137.
- [12] B.Frois, C.N.Papanicolas, and S.E.Williamson, *Modern Topics in Electron Scattering*, ed. B.Frois  
and I.Sick, World Scientific, (1991) 352.
- [13] J.L.Friar and J.W.Negele, *Nucl. Phys.*, **A212**, (1973) 93;  
*Adv. Nucl. Phys.*, **Vol.8**, (1975) 219.
- [14] G.Cowan, *Statistical Data Analysis*, Clarendon Press, Oxford, (1998).
- [15] *Maximum-Entropy and Bayesian Methods in Science and Engineering*, Vol. 1: Foundations.  
ed. G.J.Erickson and C.Ray Smith, Kluwer Academic Publishers, (1988).
- [16] A.Kohama, R.Seki, A.Arima, and S.Yamaji, *RIKEN Review*, **39**, (2001) 155.
- [17] R.J.Glauber, *Lectures in Theoretical Physics*,  
ed. W.E.Brittin and D.G.Dunham, Interscience, New York, **Vol.1**, (1959) 315; *High-Energy  
Physics and Nuclear Structure*, ed. S.Devons, Plenum Press (1970) 207.
- [18] B.Dreher, J.Friedrich, K.Merle, H.Rothhaus, and G.Luehrs,  
*Nucl. Phys.*, **A235**, (1974) 219.
- [19] J.Friedrich and N.Voegler, *Nucl. Phys.*, **A373**, (1982) 192.
- [20] J.Friedrich, N.Voegler, and P.-G.Reinhard, *Nucl. Phys.*, **A459**, (1986) 10.
- [21] M.Kamimura, *Phys. Rev.*, **A38**, (1988) 621..
- [22] F.Lenz, *Z.Phys.*, **222**, (1969) 491.
- [23] J.Friedrich and F.Lenz, *Nucl. Phys.*, **A183**, (1972) 523.
- [24] I.Sick, *Nucl. Phys.*, **A218**, (1974) 509.
- [25] V.Breton *et al.*, *Phys. Rev. Lett.*, **66**, (1991) 572.

- [26] J.M.Cavedon *et al.*, *Phys. Rev. Lett.*, **58**, (1987) 195.
- [27] Yu.N.Eldyshev, V.N.Lukyanov, Yu.S.Pol', *Sov. Jour. Nucl. Phys.*, **16**, (1973) 282.
- [28] V.V.Burov, D.N.Kadrev, V.K.Lukyanov, and Yu.S.Pol', *Phys. Atom. Nucl.*, **61**, (1998) 525.
- [29] J.R.Ficenec, W.P.Trower, J.Heisenberg, and I.Sick, *Phys. Lett.*, **32B**, (1970) 460.
- [30] I.Sick *et al.*, *Phys. Rev. Lett.*, **35**, (1975) 910.
- [31] G.D.Alkhazov *et al.*, *Phys. Lett.*, **67B**, (1977) 402-404.
- [32] G.D.Alkhazov *et al.*, *Nucl. Phys.*, **A381**, (1982) 430.
- [33] R.M.Lombard, G.D.Alkhazov, and O.A.Domchenkov, *Nucl. Phys.*, **A360**, (1981) 233.
- [34] R.D.Amado, J.P.Dedonder, F.Lenz, *Phys. Rev.*, **C21**, (1980) 647.
- [35] A.W.Thomas, *Nucl. Phys.*, **A354**, (1981) 51c.
- [36] G.D.Alkhazov, S.L.Belostotsky, and A.A.Vorobyov, *Phys. Rep.*, **42C**, (1978) 89.
- [37] A.Chaumeaux, V.Layly, and R.Schaeffer, *Ann. Phys.*, **116**, (1978) 247.
- [38] I.Brissaud and M.K.Brussel, *Phys. Rev.*, **C15**, (1977) 452.
- [39] L.Ray, W.Rory Coker, and G.W.Hoffmann, *Phys. Rev.*, **C18**, (1978) 2641.
- [40] L.Ray, *Phys. Rev.*, **C19**, (1979) 1855.
- [41] G.W.Hoffmann *et al.*, *Phys. Rev.*, **C21**, (1980) 1488.
- [42] V.E.Starodubsky and N.M.Hintz, *Phys. Rev.*, **C49**, (1994) 2118.
- [43] H.J.Gils, H.Rebel, and E.Friedman, *Phys. Rev.*, **C29**, (1984) 1295.
- [44] G.D.Alkhazov *et al.*, *Phys. Rev. Lett.*, **78**, (1997) 2313.
- [45] R.Seki and I.Tanihata, unpublished.
- [46] F.Maréchal *et al.*, *Phys. Rev.*, **C60**, (1999) 034615.
- [47] H.Scheit *et al.*, *Phys. Rev.*, **C63**, (2000) 014604.
- [48] I.Tanihata *et al.*, *Phys. Lett.*, **B287**, (1992) 307; *Phys. Lett.*, **B289**, (1992) 261.
- [49] A.Ozawa *et al.*, *Nucl.Phys.*, **A691**, (2001) 599.
- [50] A.Ozawa, T.Suzuki, and I.Tanihata, *Nucl. Phys.*, **A693**, (2001) 32.
- [51] F.James, MINUIT, Reference Manual, Ver. 94.1, CERN Program Library Long Writeup **D506**, (1994).
- [52] R.Glauber and G.Matthiae, *Nucl. Phys.*, **B21**, (1970) 135.
- [53] W.Czyż, L.Leśniak, and W.Wolek, *Nucl. Phys.*, **B19**, (1970) 125.
- [54] H.DeVries, W.DeIager, and C.DeVries, *Atomic Data and Nuclear Data Tables*, **36**, (1987) 495.
- [55] J.Borysowicz and J.H.Hetherington, *Phys.Rev.*, **C7**, (1973) 2293.
- [56] J.H.Hetherington and J.Borysowicz, *Nucl. Phys.*, **A219**, (1974) 221.



- [57] J.W.Lightbody, Jr. *et al.*, *Phys.Rev.*, **C27**, (1983) 113.
- [58] J.Meng, I.Tanihata, and S.Yamaji, *Phys.Lett.*, **B419**, (1998) 1.
- [59] S.Shlomo and R.Schaeffer, *Phys. Lett.*, **83B**, (1979) 5.
- [60] K.Varga, S.C.Pieper, Y.Suzuki, and R.B.Wiringa, *nucl-th/0205027*.
- [61] E.Hiyama and M.Kamimura, *Nucl. Phys.*, **A588**, (1995) 35c.
- [62] J.Bystricky *et al.*, *LANDOLT-BÖRNSTEIN. New Series.*, I/9a (1980).

Fig. 1

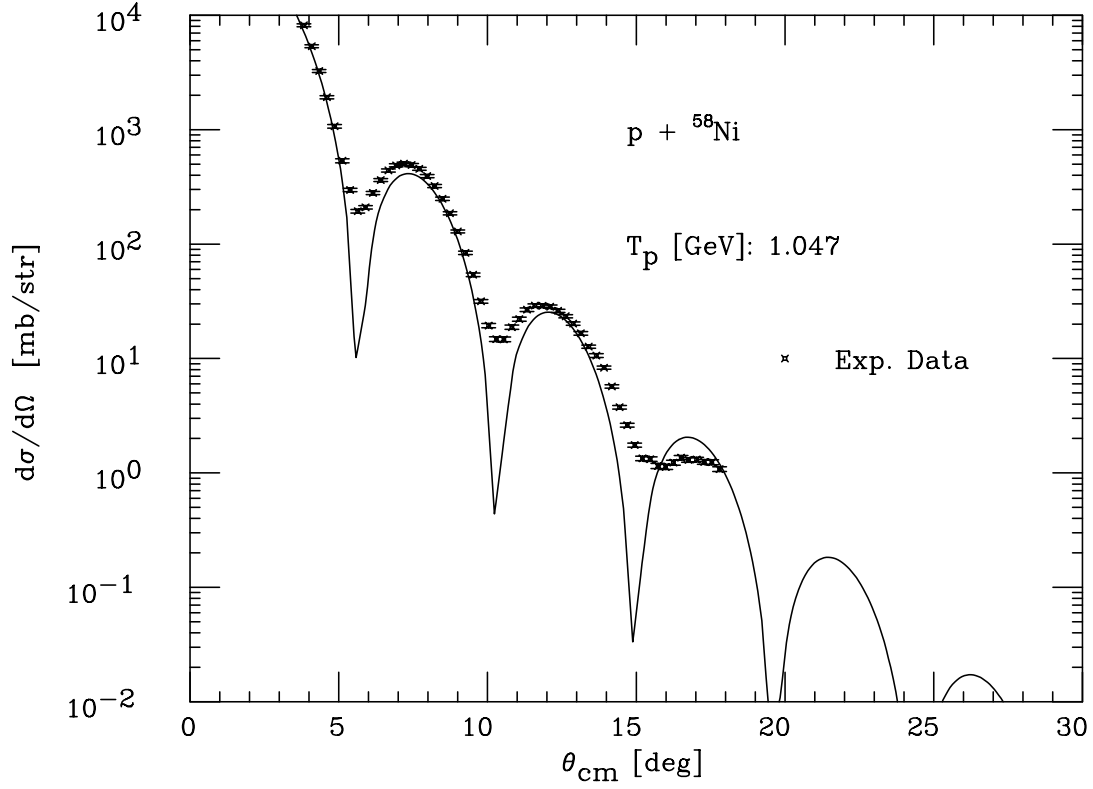


Figure 1: Comparison of the theoretical cross section with the real experimental data. The solid curve is the theoretical cross section of the proton- $^{58}\text{Ni}$  elastic scattering without the Coulomb interaction. The crosses with bar are the experimental data of SATURN at Saclay. The kinetic energy of the incident proton is 1.047 [GeV].

Fig. 2a)

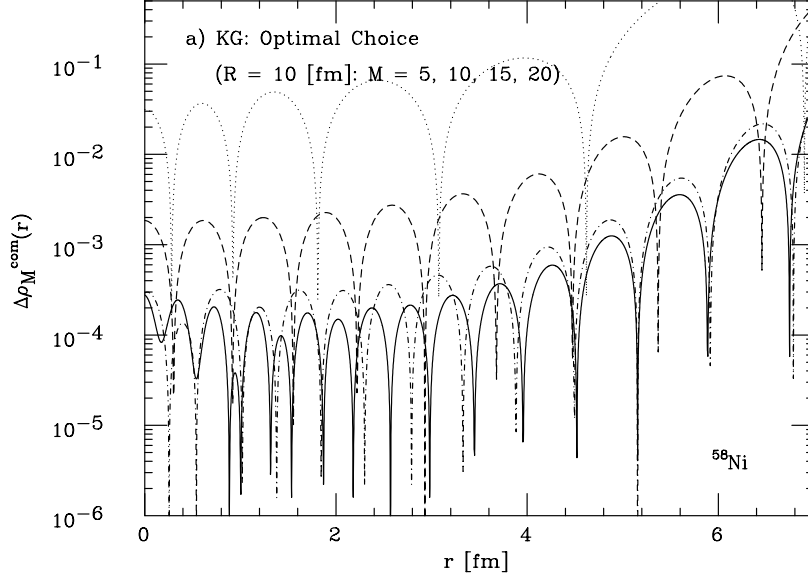


Fig. 2b)

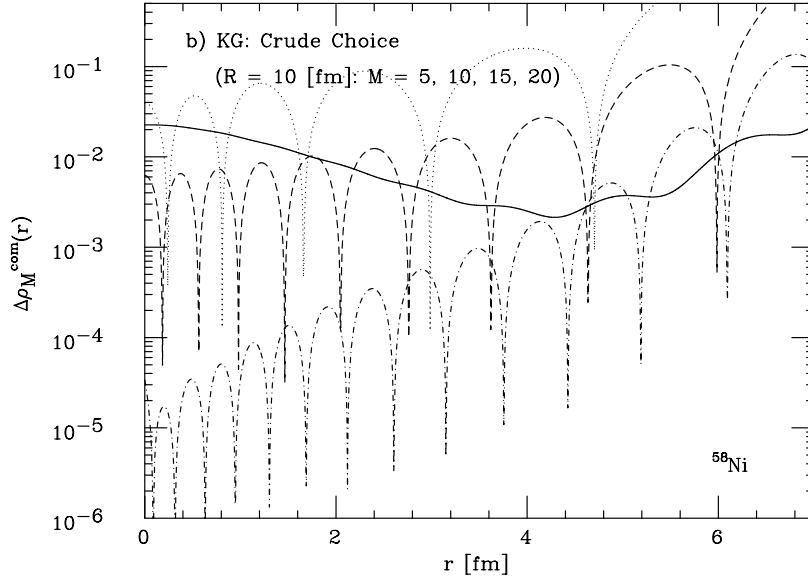


Figure 2:  $M$ -dependence of the completeness error of the Kamimura-Gauss (KG) basis functions a) with the best-fit parameters, b) with a crude choice of  $r_1$  and  $r_M$ , for  $M = 5, 10, 15$ , and  $20$ .  $R = 10$  [fm]. The dotted curve is for  $M = 5$ , the dashed one is for  $M = 10$ , the dash-dotted one is for  $M = 15$ , and the solid one is for  $M = 20$ .

Fig. 3

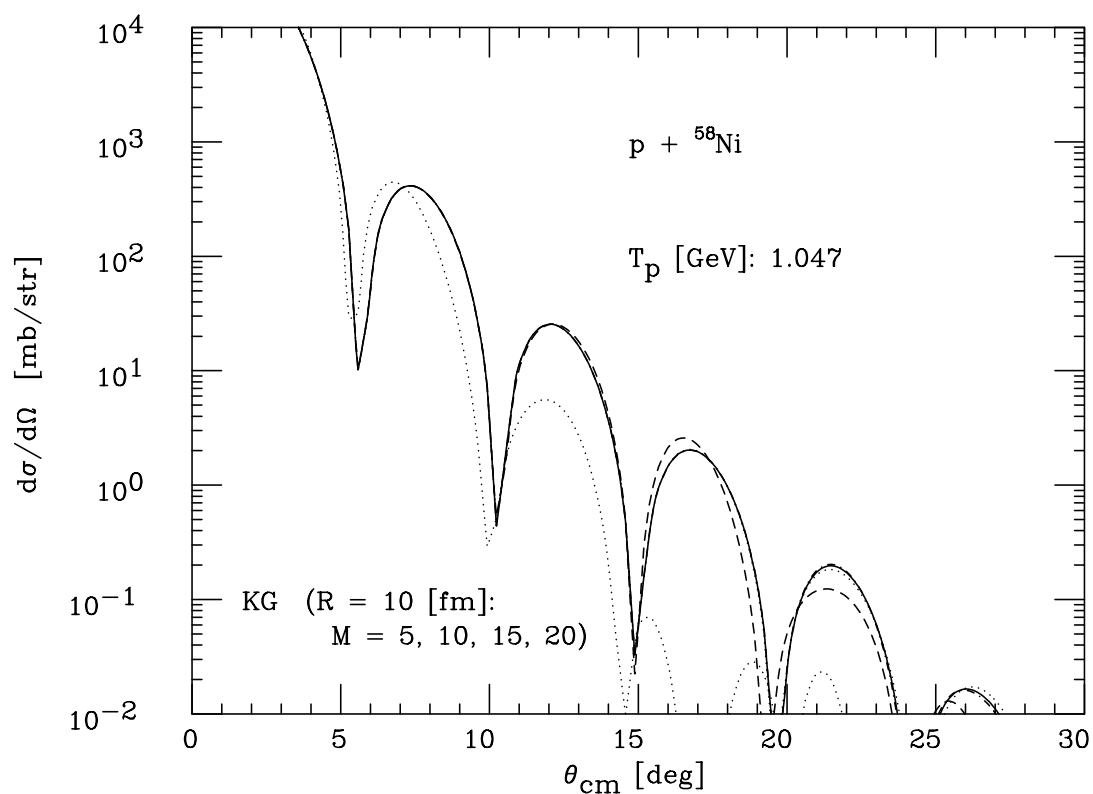


Figure 3:  $M$ -dependence of the cross section with the Kamimura-Gauss (KG) basis functions for  $M = 5, 10, 15$ , and  $20$ .  $R = 10$  [fm]. The dotted curve is for  $M = 5$ , the dashed one is for  $M = 10$ , the dash-dotted one is for  $M = 15$ , and the solid one is for  $M = 20$ . Another dotted curve, as it is quite difficult to be seen, is obtained by using the original  $\rho_{\text{true}}(r)$ .

Fig. 4

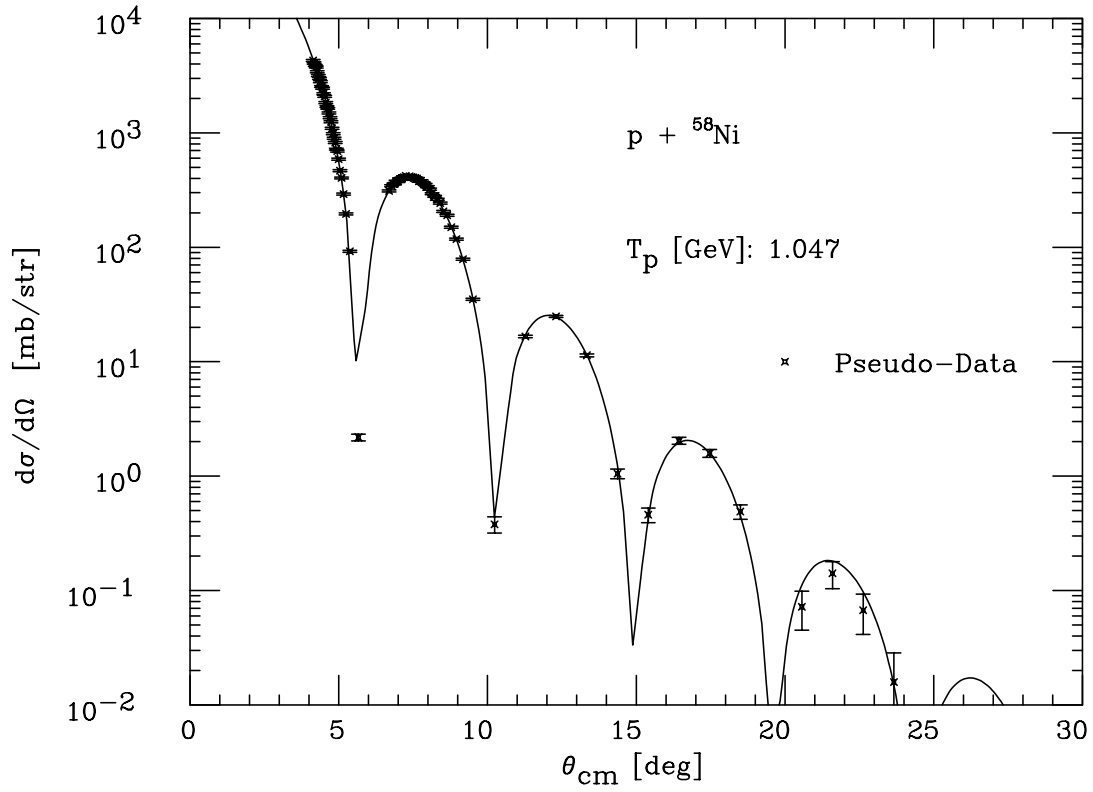


Figure 4: An example of pseudo-data set of the pseudo-data-set group (PDSG) A. Those simulate a series of measurements of the cross section of proton- ${}^{58}\text{Ni}$  elastic scattering. The solid curve is obtained by using the original  $\rho_{\text{true}}(r)$ .

Fig. 5a)

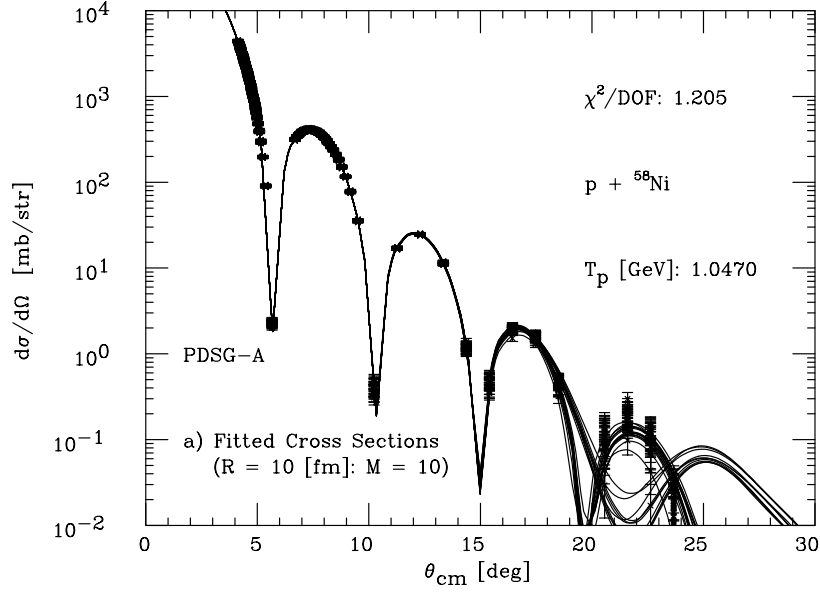


Fig. 5b)

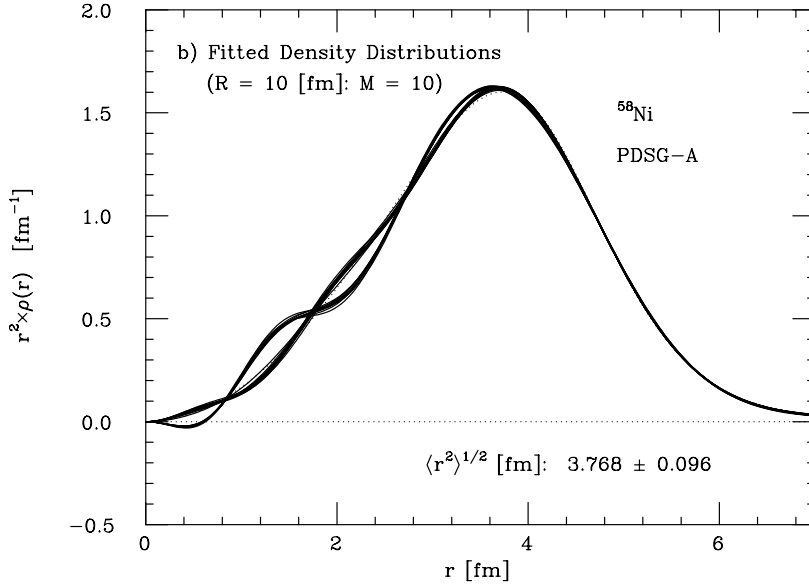


Figure 5: Results of the least-square fitting for the pseudo-data-set group (PDSG) A of  $^{58}\text{Ni}$ .  $R = 10$  [fm] and  $M = 10$ . a) 25 fitted cross sections (solid curve) and all the pseudo-data (cross with bar). b) 25 fitted density distributions (solid curve), and the original distribution (dotted curve). The density distributions are drawn in the form of  $r^2 \rho(r)$ .

Fig. 6a)

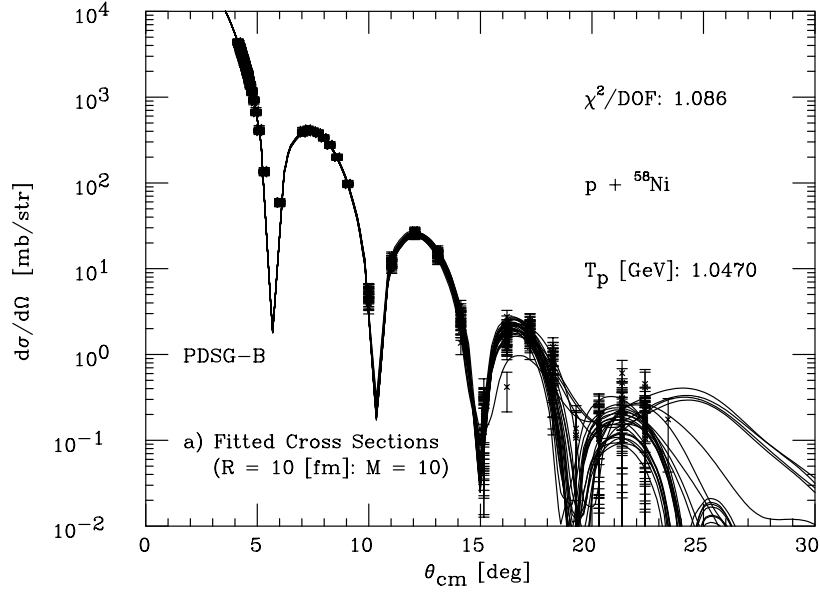


Fig. 6b)

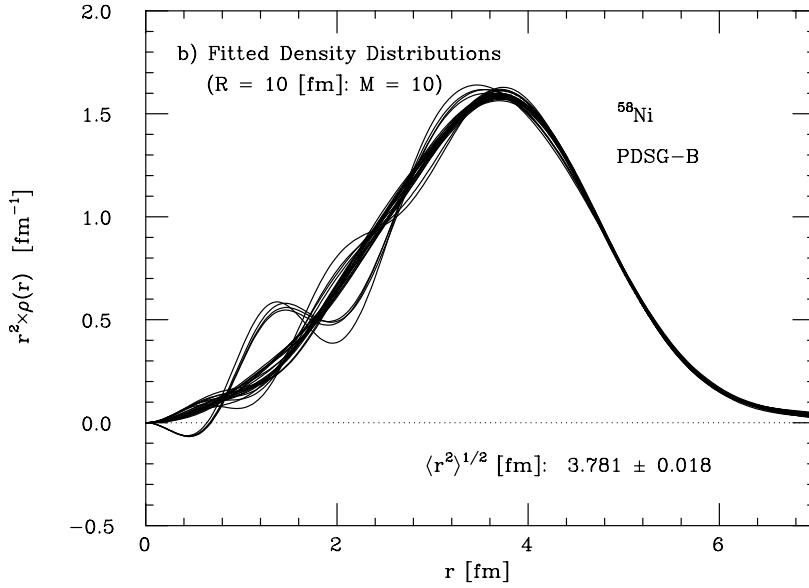


Figure 6: Results of the least-square fitting for the pseudo-data-set group (PDSG) B of  ${}^{58}\text{Ni}$ .  $R = 10$  [fm] and  $M = 10$ . a) and b) are the same as Fig. 5.

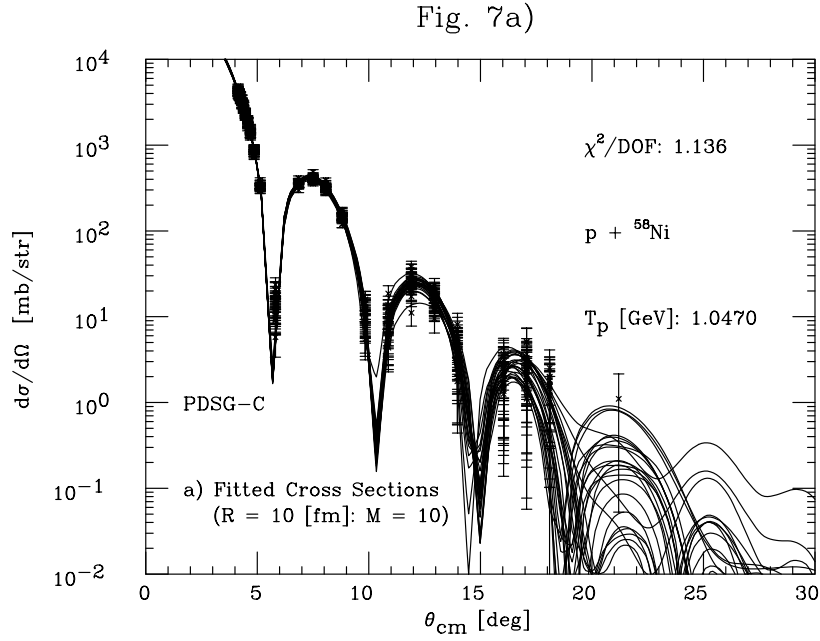


Figure 7: Results of the least-square fitting for the pseudo-data-set group (PDSG) C of  $^{58}\text{Ni}$ .  $R = 10$  [fm] and  $M = 10$ . a) and b) are the same as Fig. 5.



Fig. 8a)

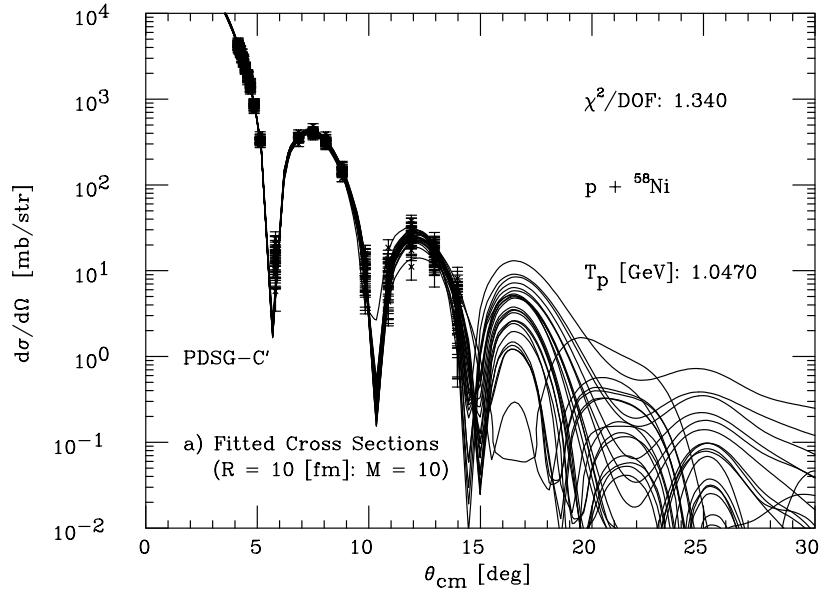


Fig. 8b)

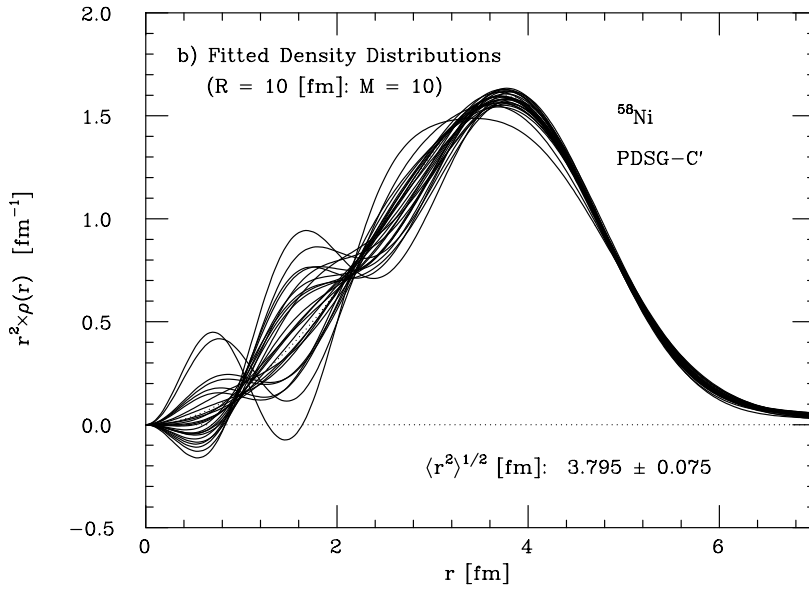


Figure 8: Results of the least-square fitting for the pseudo-data-set group (PDSG) C' of  $^{58}\text{Ni}$ .  $R = 10$  [fm] and  $M = 10$ . a) and b) are the same as Fig. 5.

Fig. 9a)

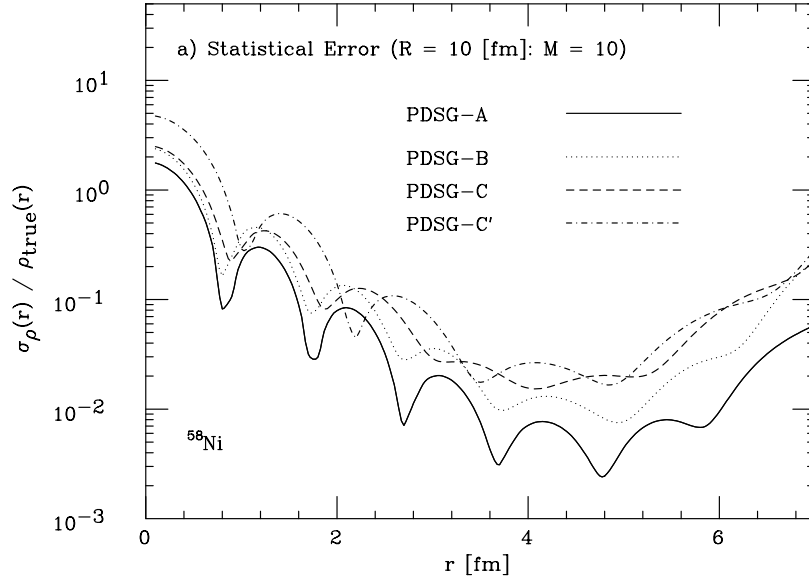


Fig. 9b)

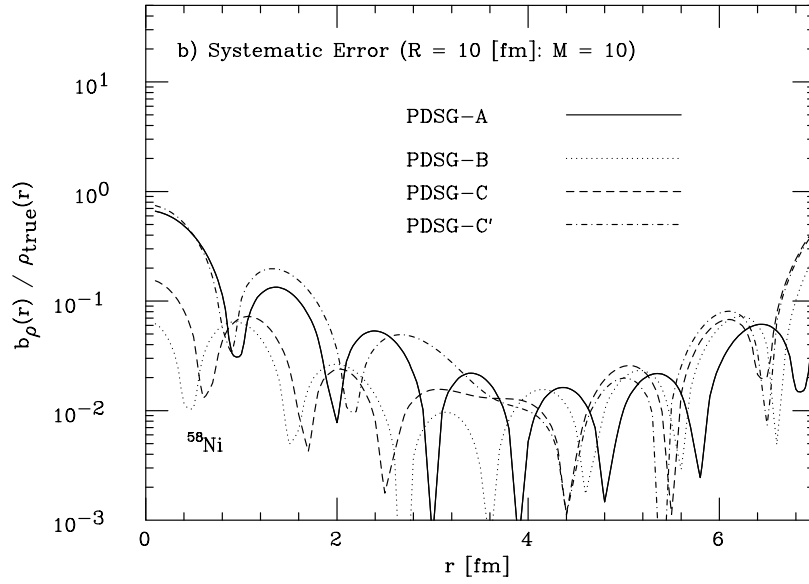


Figure 9: a) Statistical error, and b) systematic error of the fitted density distributions for  $^{58}\text{Ni}$ . We divide them by  $\rho_{\text{true}}(r)$  at each  $r$ . The solid curve is for the pseudo-data-set group (PDSG) A, the dotted one is for the group B, the dashed one is for the group C, the dash-dotted one is for the group C'.

Fig. 10a)

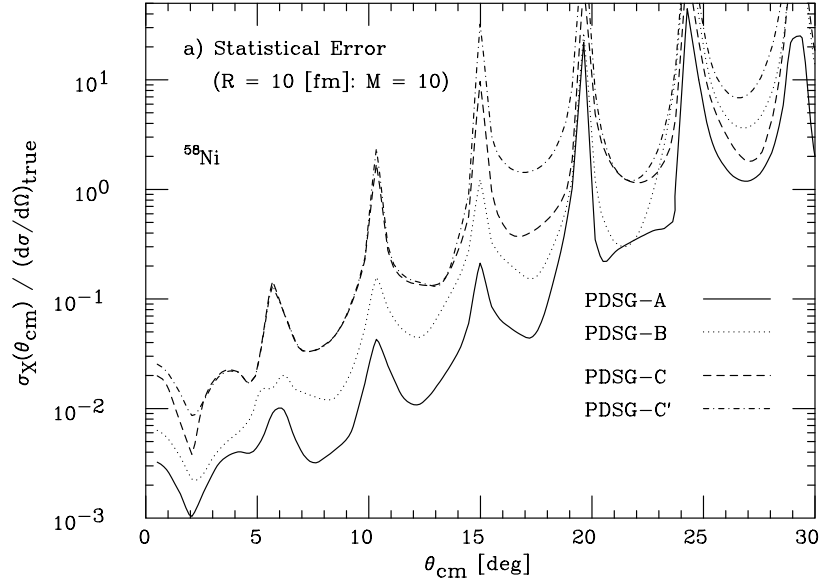


Fig. 10b)

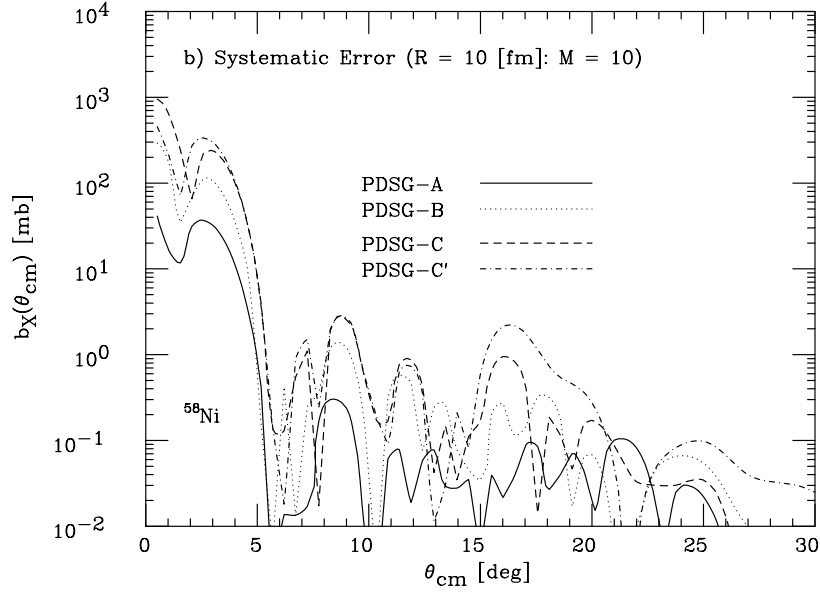


Figure 10: a) Statistical error, and b) systematic error of the fitted cross sections for  $^{58}\text{Ni}$ . The curves are the same as in Fig. 9.

Fig. 11a)

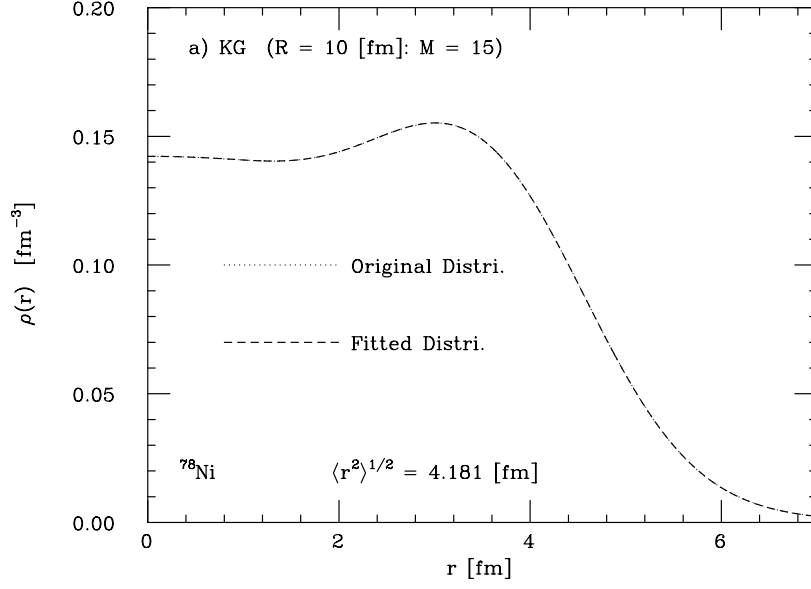


Fig. 11b)

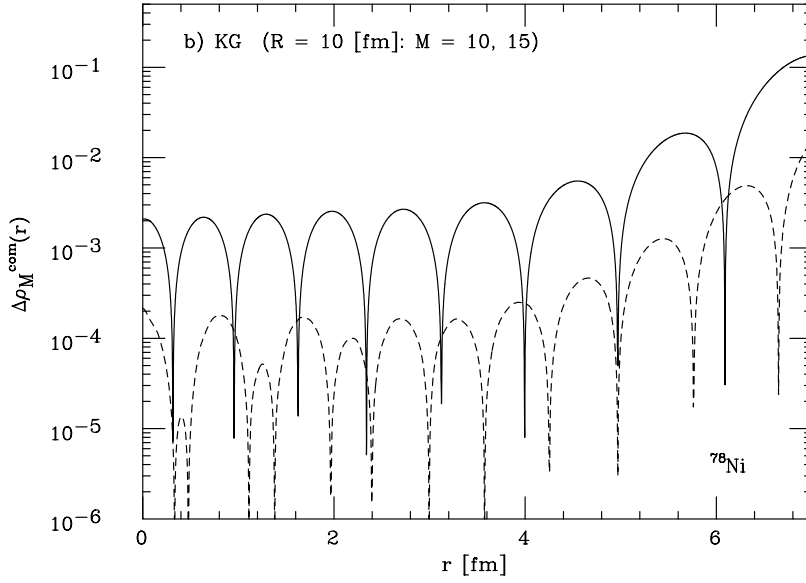


Figure 11: a) Matter density distribution of  $^{78}\text{Ni}$ . The dotted curve is the original density distribution obtained in the relativistic mean-field theory.  $R = 10$  [fm] and  $M = 15$ . The dashes curve is obtained by fitting of the Kamimura-Gauss (KG) basis functions. b) Completeness error of  $^{78}\text{Ni}$  for  $M = 10$  and  $15$ . The solid curve is for  $M = 10$ ,  $r_1 = 1.0$  [fm] and  $r_M = 5.5$  [fm] (Table 1). The dashed curve is the case of  $M = 15$ ,  $r_1 = 0.7$  [fm] and  $r_M = 5.6$  [fm] (Table 1).

Fig. 12a)

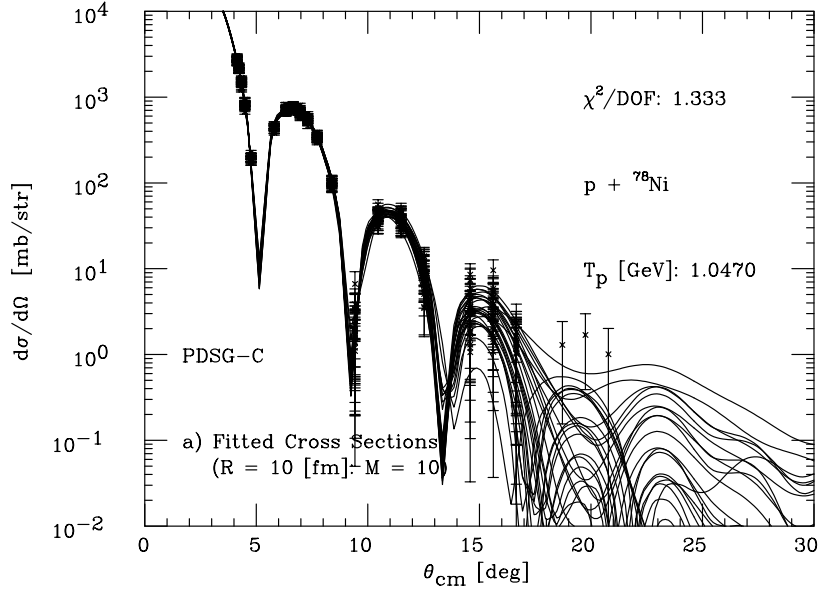


Fig. 12b)

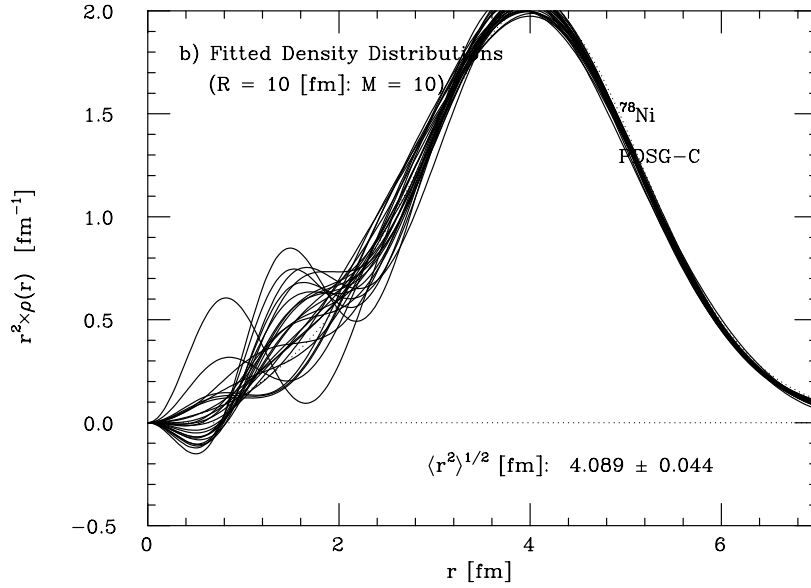


Figure 12: Results of the least-square fitting for the pseudo-data-set group (PDSG) C of  $^{78}\text{Ni}$ .  $R = 10$  [fm] and  $M = 10$ . a) and b) are the same as Fig. 5.

Fig. 13

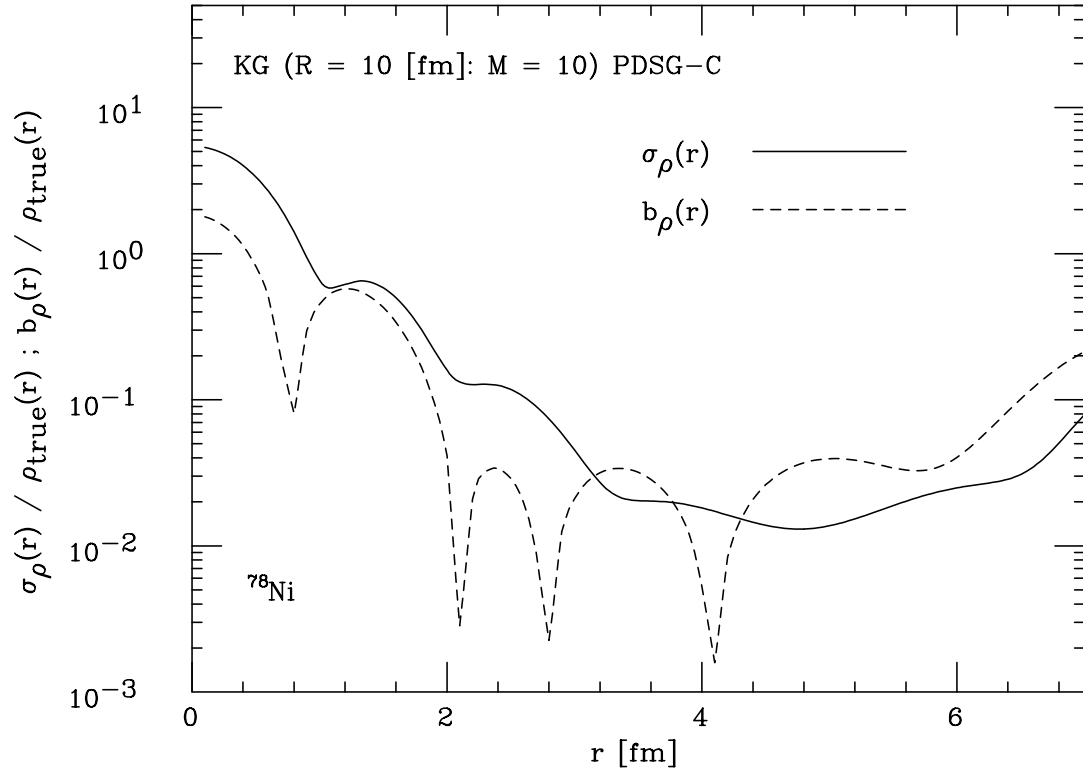


Figure 13: Statistical error and systematic error of the fitted density distributions for  $^{78}\text{Ni}$ . The solid curve is the statistical error and the dashed one is the systematic error. They are divided by  $\rho_{\text{true}}(r)$ .

Fig. 14a)

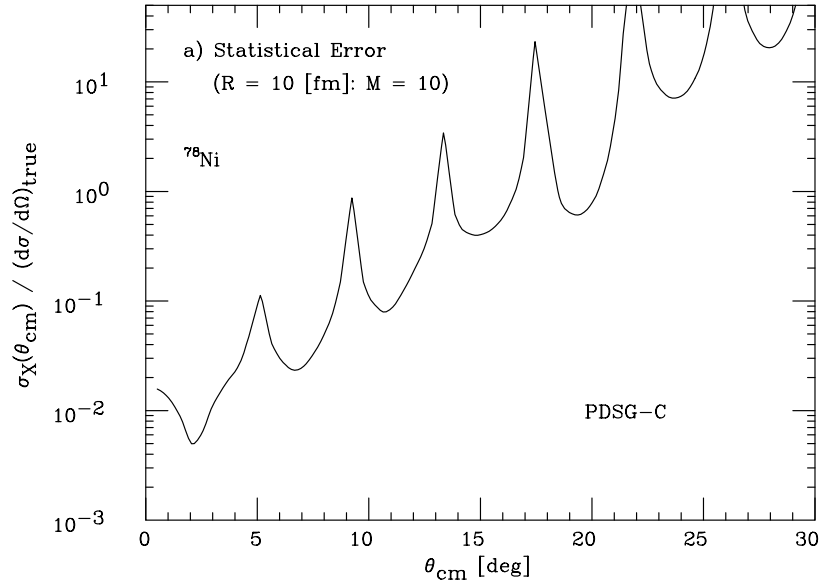


Fig. 14b)

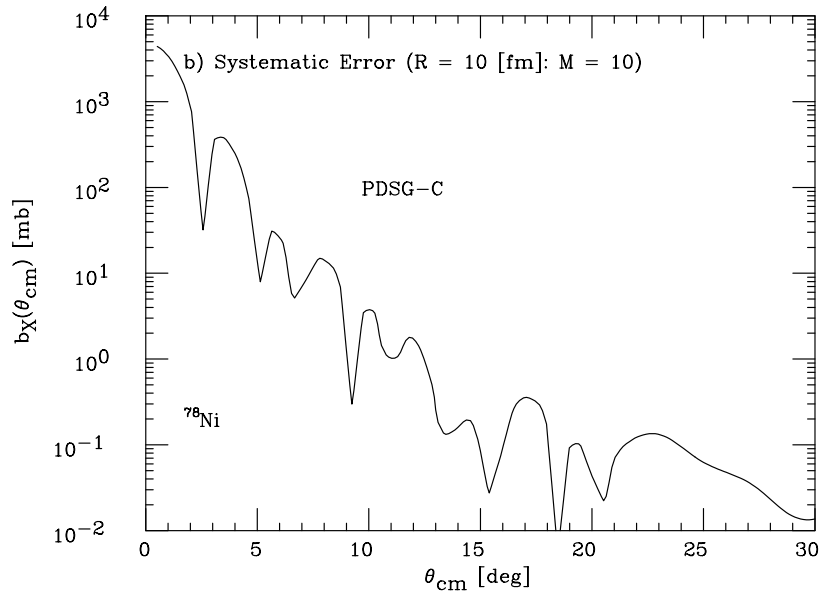


Figure 14: a) Statistical error, and b) systematic error of the fitted cross sections for  $^{78}\text{Ni}$ .

Fig. 15

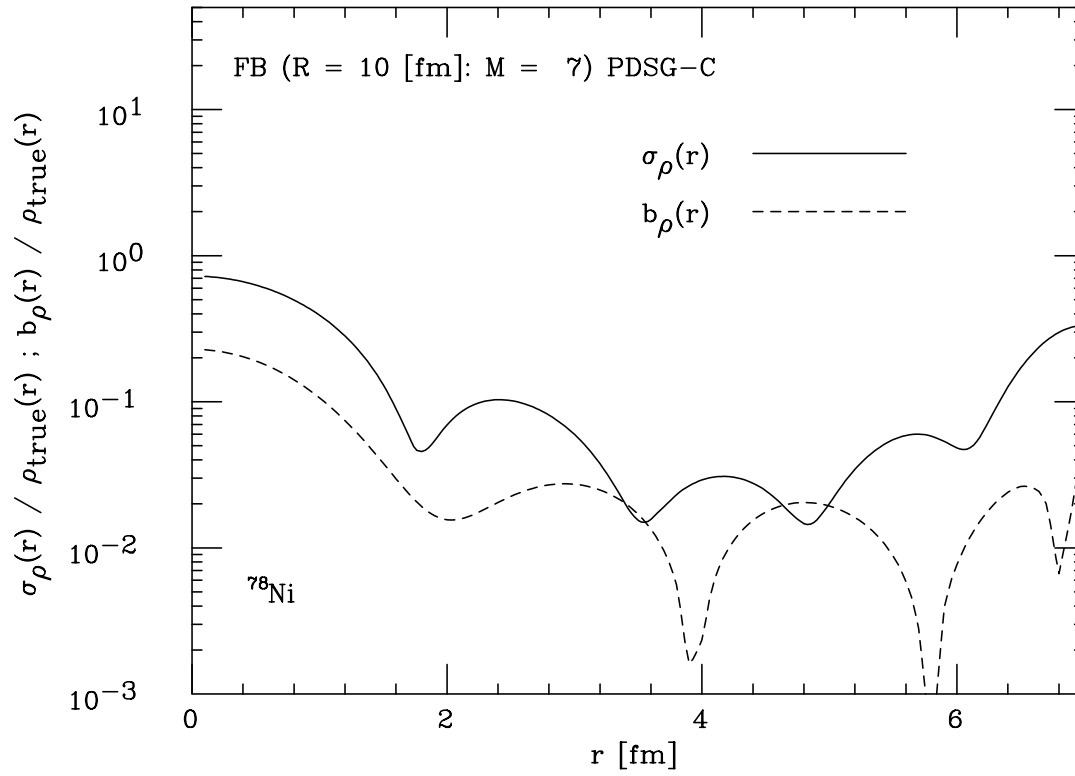


Figure 15: Statistical error and systematic error of the fitted density distributions for  $^{78}\text{Ni}$  for the Fourier-Bessel (FB) basis functions. The curves are the same as in Fig. 13.



Fig. 16a)

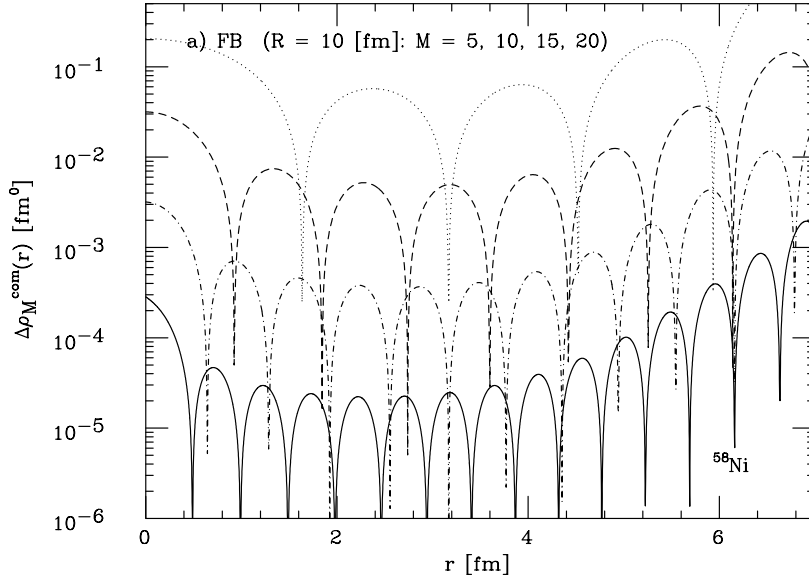


Fig. 16b)

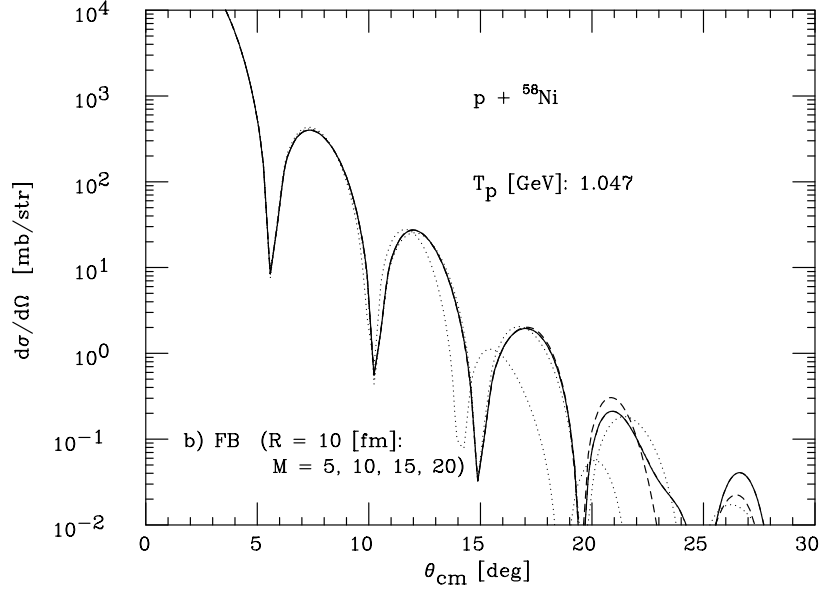


Figure 16:  $M$ -dependence of a) the completeness error of the Fourier-Bessel (FB) basis functions and of b) the cross section with the same basis functions for  $M = 5, 10, 15$ , and  $20$ .  $R = 10$  [fm]. The dotted curve is for  $M = 5$ , the dashed one is for  $M = 10$ , the dash-dotted one is for  $M = 15$ , and the solid one is for  $M = 20$ . Another dotted curve in b), as it is quite difficult to be seen, is obtained by using the original  $\rho_{\text{true}}(r)$ . The curves are the same as in Figs. 2 and 3.